Brass Wire Forming By Friction Stir Back Extrusion: Numerical Modeling and Experiment

Mostafa Akbari (✉ mr.mostafaakbari@yahoo.com)
  Technical and Vocational University

Parviz Asadi
  Technical and Vocational University

Brass Wire Forming by Friction Stir Back Extrusion: Numerical Modeling and Experiment

Mostafa Akbari[1,*], Parviz Asadi[1]

[1]*Department of Mechanical Engineering, Faculty of Karaj, Alborz Branch, Technical and Vocational University (TVU), Iran*

[2]*New Product Development (NPD), Iran Khodro Co., Tehran, Iran*

[2]*Department of Mechanical Engineering, Faculty of Engineering, Imam Khomeini International University, Qazvin, Iran.*

Abstract

Friction stir back extrusion (FSBE) is used to produce brass wires and then, Numerical modeling is developed to simulate the FSBE of brass based on the Coupled Eulerian-Lagrangian technique (CEL) and verified by experiments. Next, the effects of FSBE parameters such as tool rotational and plunging speed on the strain and temperature distributions, microstructure, and patterns of material flow are studied. The results show that, the highest temperature and strain occurs near the tool/workpiece interface, but in a further distance from the tool axis. Additionally, in the cross section of a FSBE wire, the microstructure is finer in the periphery of the sample. A higher rotational speed or a lower plunging speed results in a coarser microstructure. The material flow pattern during the process is conical helix, and does not change meaningfully by the process parameters. The points at the further distance from the tool axis, along with an upward movement, experience an inward spiral movement which is amplified by higher rotational speed. However, the materials very near the tool axis almost take an upward movement and endure a very lower strain.

---

[*] Corresponding Author: Room 442- Department of Mechanical Engineering, Faculty of Engineering, Imam Khomeini International University, Qazvin, Iran. Postal Code: 3414896818.
Emails: asadi@eng.ikiu.ac.ir; parvizasadi@ut.ac.ir

1. Introduction

The brasses (Cu–Zn alloys) contain 5 to 45% of zinc to donate a higher hardness and mechanical resistance to the brass, while the rest is copper giving a higher corrosion resistance for many mediums [1], [2]. Therefore, these alloys have various mechanical and physical properties based on their Zn content. Also, they may have a small amount of iron, lead and other trace elements. Furthermore, brasses have high thermal and electrical conductivities, high malleability, good combination of strength and ductility, high corrosion resistance, good castability and formability and excellent machinability [2], [3]. These excellent and special properties have widespread the applications of brasses in different fields such as low pressure valves, plumbing fittings and fixtures, counters and taps, bearings, gears, architectural frames and decorative hardware, musical instruments, germicidal and anti-microbial devices [4], [5].

Due to the limited resources, high energy consumption and environmental contamination, the metals recycling has become an essential topic these days. The copper, aluminum, iron, etc. based metals and alloys are broadly utilized in production to manufacture almost all kinds of industrial products. Therefore, the metal chips produced during machining are the majority of waste materials in the industrial firms [6]. Additionally, every year, a large amount of metal scrap pieces is produced in the shops which then are chopped up with shredders into chips. Although these wastes are mostly polluted with the oils and cutting fluids, the washing costs are very lower than mining them. Generally, for recycling, the metal chips are re-casted [6], [7]. In this way some companies are needed for collecting the chips and transferring them into the casting shops and again rolling, extrusion and other processes are required to produce the final/usable metal product. However, by the technology advancement, new recycling techniques have been emerged such as the Friction Stir Back Extrusion (FSBE) enabling the shops to directly recycle the metal chips into extruded products.

Previously, the friction based processes such friction welding methods have demonstrated their capability in joining and forming the materials in solid state and have introduced products with desired mechanical properties [8], [9]. Recently a new friction stirring concept was developed, which targets the recycling and processing of chips to generate a bulk material. The FSBE as a solid state recycling technic, produces frictional heat to soften the recycling chips and then, by applying adequate pressure as a forging force, the chips are merged and pushed to a channel to produce an integrated product like a wire or tube.

Abu-Farha [10] applied FSBE process to produce aluminum tubes and observed fine-grained microstructure along the tube wall. Dinaharan et al. [11] explained how the FSBE can be applied to deform the solid cylindrical pure copper ingots to defect-free tubes. Their microstructural observations showed that the produced copper tubes belong homogenous microstructure along the tube, but the trapped frictional heat made the grains coarse. So, they concluded that an adequate heat dissipation during FSBE is required to control the evolution of microstructure. Similarly, Mathew et al. [12] produced aluminum seamless tubes by deforming the solid cylindrical bars utilizing the FSBE. They indicated this process is capable to produce defect-free aluminum seamless tubes. Zhang et al. [13] deformed hollow cylindrical billets of 6063-T6 aluminum alloy to tubes by FSBE and found equiaxed refined grain structure as a result of dynamic recrystallization. They reported that the grain size is reduced from ~58 µm in the base metal to 20.6 µm at the inner wall of tube. However, the microhardness is declined from 100 to 60–75 HV due to the process thermal cycle.

In terms of finite element modeling (FEM) of FSBE some endeavors are reported in the literature in recent years. Behnagh et al. [14] presented a 2D thermo-mechanically coupled Eulerian–Lagrangian model using Abaqus software to simulate the FSBE process for production of pure magnesium alloy wires, while the work hardening and strain softening effects were taken into consideration in the model. Additionally, they modeled grain size evolution based on the dynamic recrystallization (DRX) kinetics laws. Baffari et al. [15] proposed a 3D Lagrangian thermo-mechanically coupled numerical model using DEFORM3D software for FSBE of AZ31 magnesium wire and approved the model by temperature measurements. They also investigated the process mechanics to attain information on the material flow over the process as well as on the final product surface quality as a function of the tool plunging force and rotational speed. Additionally, in another work [16], they investigated the effect of process parameters and extrusion rate on the temperature and strain distribution.

In the present research, a brass shaft is formed using FSBE to produce integrated solid wires and the effects of rotational and plunging speeds on the microstructure and mechanical properties of produced brass wires are investigated. Additionally, Coupled Eulerian Lagrangian (CEL) model is proposed to numerically simulate the FSBE process for brass wire production. The model is validated based on the acquired experimental temperature data and then, the effects of process parameters on the temperature and strain distributions as well as the material flow patterns are investigated.

2. Experimental procedure

In the present work, a CuZn39Pb2Sn brass shaft, with the chemical composition listed in Table 1, was inserted in the mold cavity (matrix) prior to applying the FSBE process. The matrix was made from H13 hot working steel and then heat treated to attain 52 RC hardness (Fig. 1a). The FSBE tool, with the outer and inner diameters of 30 and 7 mm, was made of Chrome-Nickel steels and heat treated to achieve 58 RC hardness. The FBE tool picture are shown in Fig. 1b. In the present work the tool and matrix dimensions were constant but the main process parameters of tool rotational and plunging speeds were varied to observe their effects on the mechanical and microstructural properties of produced brass wires. The rotational and plunging speeds were varied between 315-800 rpm, and 25-40 mm/min, respectively. Some of the produced brass wires by FSBE process are shown in Fig. 1c.

To acquire the temperature history during the process, a four-channel thermometer was used and the thermocouples were inserted in the radial 4-mm holes on the matrix body with different spaces from the top edge.

For microstructural observations on the optical microscope (OM), the wires are cut in perpendicular to wire axis and then, polished using a standard procedure. The prepared metallographic samples are etched with a solution of 5 g Fe_3Cl, 30 mL HCl and 100 mL ethanol in 20 seconds and then washed with distilled water and dried.

Table 1. Chemical compositions of CuZn39Pb2Sn brass used in this study.

Element	Cu	Zn	Pb	Sn	Fe	Ni	Al	Mn	Si	S	P
% wt.	58.9	37.39	2.14	0.60	0.51	0.43	0.007	0.004	0.003	0.003	0.003

(a)

(b)

(C)

(c)

Fig. 1. (a) The matrix with its dimensions, (b) the tool with its dimensions, and (c) some of the produced 7-mm-diameter wires produced by FSBE.

3. Model description

The ABAQUS software was utilized to simulate the material flow and temperature history during the FSBE of brass. A CEL method is utilized in this study to simulate various aspects of process. In this method the finite elements are fixed in space, while the material could flow through these elements.

As a result, there is no mesh distortion that usually existed in the Lagrangian methods. The workpiece is defined as an Eulerian part with EC3D8RT elements and the tool was modeled as a rigid Lagrangian body. The Eulerian part has been considered as a cylindrical shape that includes two sub-regions: "full" and "void". The lower region "full" is predefined with the brass, and no material is assigned in the upper region "void" to identify the movement of the material during the process. The material layout used in the present model to produce the brass wires is shown in Fig. 2.
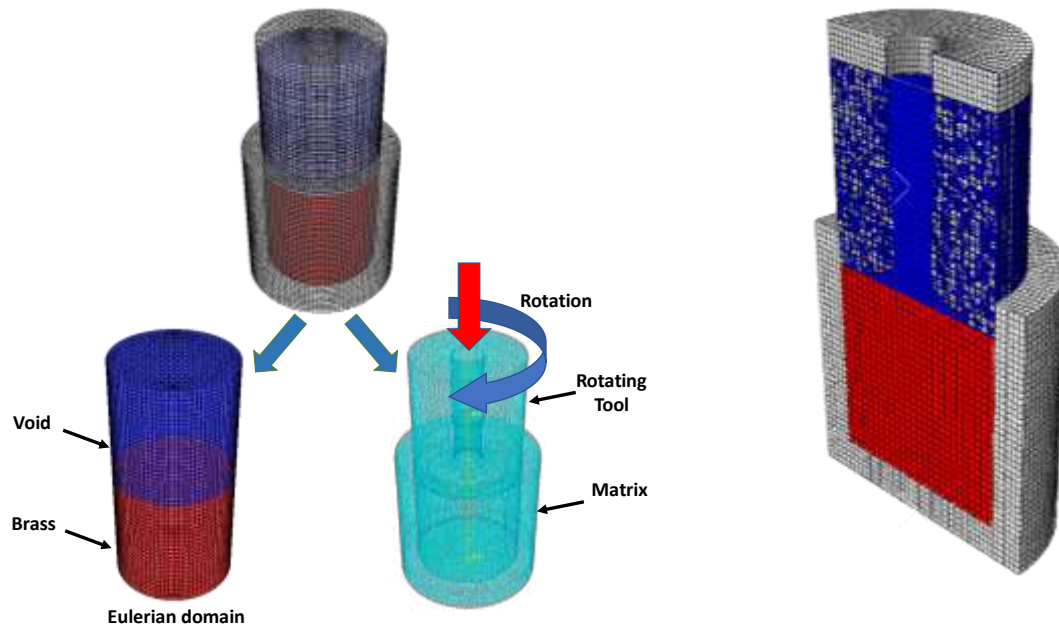

Fig. 2. The material layout used in the present model for FSBE to produce the brass wires.

3.1. Governing equations

In the CEL method developed in this investigation, Eulerian formulation, where mass, energy, and momentum are conserved, is utilized to model the workpiece domain.

The mass conservation equation (Eq. 1) represents the rate of outflow mass and mass changes inside the control volume.

$$\frac{\partial \rho}{\partial t} + \nabla.(\rho v) = 0 \tag{1}$$

where ρ and v is density and velocity of the material respectively. The conservation equation for momentum (Eq. 2) equals the change of momentum of the domain to the sum of the spatial time derivative of the gravitational force and the Cauchy stress tensor.

$$\rho(\frac{\partial v}{\partial t} + \nabla.(v \otimes v)) = \nabla.\sigma + \rho g \tag{2}$$

where, σ and g is the Cauchy stress tensor and the gravity constant. The energy conservation equation incorporates the rate of plastic work done on any element, the heat flux into elements as a result of conduction, and generation of the volumetric heat from the element.

$$\rho C_p (\frac{\partial T}{\partial t} + v.\nabla T) = \nabla.(K \nabla T) + \nabla.(\sigma.v) + \dot{Q} \tag{3}$$

where K, Cp, T and $Q\dot{}$ represent the thermal conductivity; the material specific heat, the temperature in Kelvin scale; and the rate of volumetric heat generation. The Eulerian based equations (Eqs. 1-3) have a general conservation form as below:

$$\frac{\partial \phi}{\partial t} + \nabla.\Phi = S \tag{4}$$

where, S and Φ are the source term and the flux function, respectively. Operator splitting algorithm splits the governing equation (Eq. 4) into Eulerian step containing the flux function term Φ and Lagrangian step containing the source term S, as shown in Eqs. 5 and 6. The CEL method solved these two equations sequentially. Fig. 3 schematically illustrates the split operator for each step of CEL method.

$$\frac{\partial \varphi}{\partial t} = S \tag{5}$$

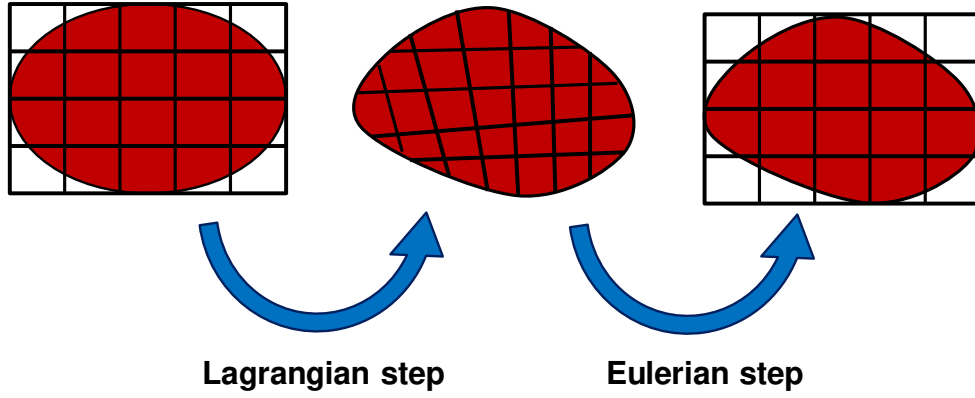$$\frac{\partial \varphi}{\partial t} + \nabla.\Phi = 0 \tag{6}$$

Fig. 3. Schematic illustration of the split operator in CEL method.

3.2. Material model

The material flow stress in FSBE is a function of strain, strain-rate and temperature. Therefore, Johnson-Cook's model (JC) is used as the material flow model of brass as following:

$$\sigma = (A + B\varepsilon^n)(1 + C\ln\left(\frac{\dot{\varepsilon}}{\dot{\varepsilon}_0}\right))[1 - \left(\frac{(T - T_r)}{(T_m - T_r)}\right)^m] \qquad (7)$$

where A, B, C, n, and m are constants related to the material, T_m is melting temperature (from Table 2); T_r is the ambient temperature, ε represents the plastic strain; $\dot{\varepsilon}_0$, the normalizing strain rate; and $\dot{\varepsilon}$ is the effective plastic strain rate. The first term of Eq. 7 is the power law that defines the influences of plastic train on the flow stress. The second and third terms of the equation considered the effect of the strain rate and temperature, respectively. Table 2 illustrates the Johnson-Cook's parameters for brass alloys [17]–[19].

Table 2. The constants of JC model for the AA 5083 and brass alloys [17]–[19].

Material	A [MPa]	B [MPa]	C	n	m	T_{ref} [°C]	T_{melt} [°C]
Brass	112	505	0.009	0.42	1.68	25	916

3.3. Contact interactions and boundary conditions

The main sources of heat generation during FSBE are the plastic deformation and friction as shown in Eq. 8:

$$\dot{Q} = \dot{Q}_F + \dot{Q}_P \tag{8}$$

where, $\dot{Q}_F$ and $\dot{Q}_P$ is friction and plastic deformation heat generation respectively. The friction heat generation is the product of tangential stress and slip-rate at the interface, as expressed by Eq. 9. Moreover, the amount of material deformation determines the heat generation because of plastic deformation as shown in Eq. 10.

$$\dot{Q}_F = \phi(\tau_S \times \dot{\gamma}) \tag{9}$$

$$\dot{Q}_P = \eta(\sigma \times \dot{\varepsilon}) \tag{10}$$

where, σ is flow stress, ϕ is frictional heat factor, ε represents strain-rate, η is inelastic heat fraction and $\gamma\,\dot{}$ is slip-rate, respectively. For thermal analysis, the Fourier law is used as the governing equation. Thus, heat generation and conduction equations can be utilized to determine the temperature distribution.

$$k\nabla^2 T + \dot{q} = \rho c \frac{\partial T}{\partial t} \tag{11}$$

where k, t and c, are thermal conductivity of the material, time and material specific heat capacity, respectively. Moreover, heat dissipation because of convection occurred from the workpiece surfaces to the air:

$$-K\frac{\partial T}{\partial \delta_S} = \gamma_{con}(T - T_a) \tag{12}$$

where T_a and γ_{con} represents the peripheral temperature and the coefficients of heat convection. At matrix and paunch outer surfaces, a convective heat transfer coefficient is used for modeling heat natural convection heat loss. Besides the FSBE paunch /workpiece contact, there is a self-contact inside the materials under process. To consider all contacts between the workpiece and tools, General contact interaction was utilized. Moreover, the tangential and normal contact is modelled by the penalty equation and the hard contact pressure enclosure to minimize the penetration of workpiece nodes into the tool. As a result, the compressive stress at the interface can be determined. General contact formulation was utilized to define the tool/workpiece contact.

3.4. Meshing

Thermally coupled eight-node linear Eulerian brick elements (EC3D8RT) with reduced integration is utilized to mesh Eulerian domain. Fine mesh is crucial parameter to achieve accurate model of FSBE. Moreover, coarse model in CEL method leads to Eulerian material flowing through Lagrangian mesh and decrease accuracy. As different mesh size was investigated and a fine mesh with mesh size of 0.8 mm is selected (Fig. 4).

The rotating tool and the matrix are modeled as the Lagrangian rigid body and meshed with the thermally coupled 4-node 3D bilinear rigid quadrilateral elements.

All tool movement conditions are assigned with respect to the tool reference point in order to control the tool movement precisely.
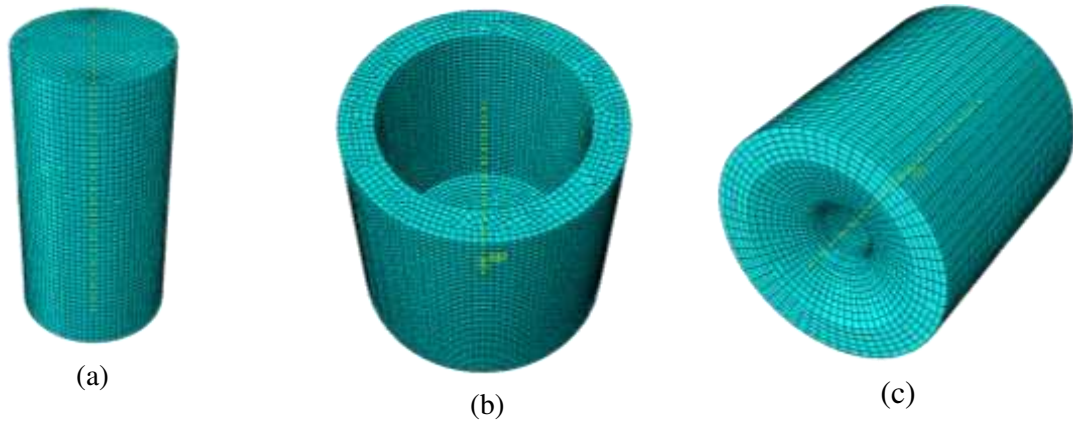

(a)

(b)

(c)

Fig. 4. Mesh in the CEL model: (a) Eulerian mesh for the workpiece, and (b) and (c) Lagrangian mesh for the tool.

4. Results

First the model is verified by the thermal history curves and then, the experimental investigations such as microstructures along with the numerical results such as temperature and strain distributions and material flow are discussed in the following subsections.

4.1. Numerical model validation

To verify the model accuracy, the simulation and experimental thermal history curves are compared (Fig. 5). The temperatures are acquired on the matrix body with 3 mm distance from the inside cylindrical surface and 10 mm distance from the top surface. Fig. 5a shows the temperature distribution on the matrix body when the tool is penetrated almost 10 mm on the matrix hole (5 mm into the workpiece) with the rotational and plunging speeds of 800 rpm and

25 mm/min. As can be seen a severe thermal gradient occurs on the matrix body and thus, its substance, not as much as rotating tool but, is important to withstand over this thermal gradient.

Fig. 5b shows the experimental and numerical temperature history curves over the process. As can be seen a good agreement is achieved between experimental and numerical results. Although the maximum temperature in the matrix body is reached almost 600 °C, it would be much higher in the tool/workpiece interface.
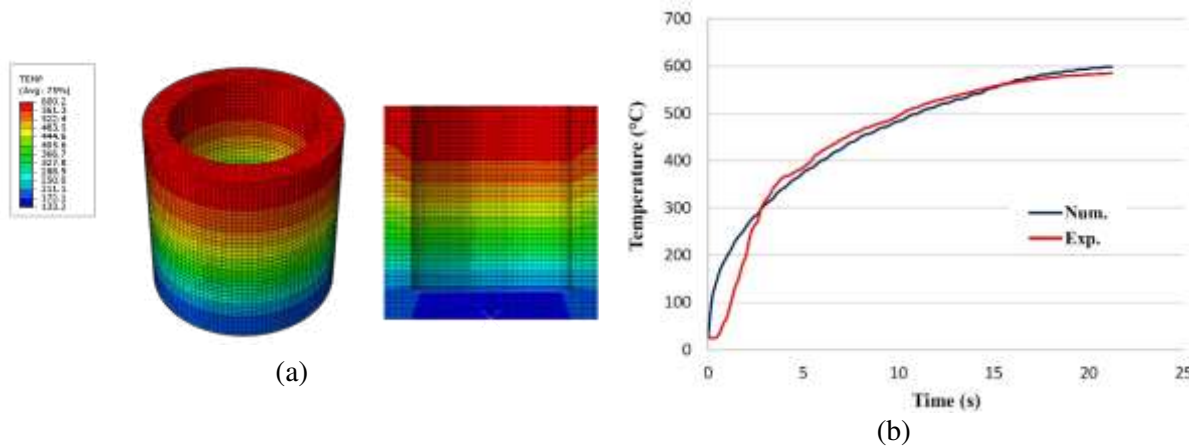

(a)

(b)

Fig. 5 (a) The temperature distribution in the matrix body over the FSBE process; the tool is penetrated 5 mm into the workpiece. (b) The experimental and numerical temperature history curves. The rotational and plunging speeds: 800 rpm and 25 mm/min.

4.2. Temperature distribution

Fig. 6 shows the temperature distribution acquired for the workpieces under extrusion by different tool rotational and plunging speeds. In the FSBE, similar to other friction-stir based processes, the required heat for material softening is mostly generated by the friction in the tool/workpiece interface. Then, by flowing the material, the plastic deformation heat is added to the total generated heat. By this generated heat, which rises the workpiece temperature up to 60-95% of substance melting point, the material is softened [20]–[22]. Then the axial movement is applied to the tool to deform the workpiece and reduce its diameter from extrusion chamber diameter (matrix cavity of 30 mm) to the wire diameter (7 mm).

It should be noticed that, the plastic deformation, similar to the friction, mostly occurs near the interface. Therefore, as can be seen in Figs. 6a-6f, the maximum temperature appears in the interface. Additionally, along the interface there is a bit temperature difference between the outer edge of the tool (diameter of 30 mm) and inner one (diameter of 7 mm). Because the

linear velocity is higher at the outer diameter both the frictional heat and the plastic deformation heat is expected to be more severe going from the center to the outer diameter.

The effects of tool rotational and plunging speeds on the temperature distribution are clearly shown in Fig. 6. By increasing the plunging speed from 25 to 40 mm/min while the rotational speed is constant on 800 rpm, the maximum temperature drops down from 860 to 780 °C (Figs. 6a-6c).

On the other hand, the rotational speed is changed from 800 to 315 rpm at the constant plunging speed of 25 mm/min and the results are demonstrated in Figs. 6a and 6d-6f. By reducing the rotational speed, generation of both the frictional and plastic deformation heat diminishes. It is shown that the maximum temperature is declined from 860 to 650 °C by decreasing the rotational speed from 800 to 315 rpm.
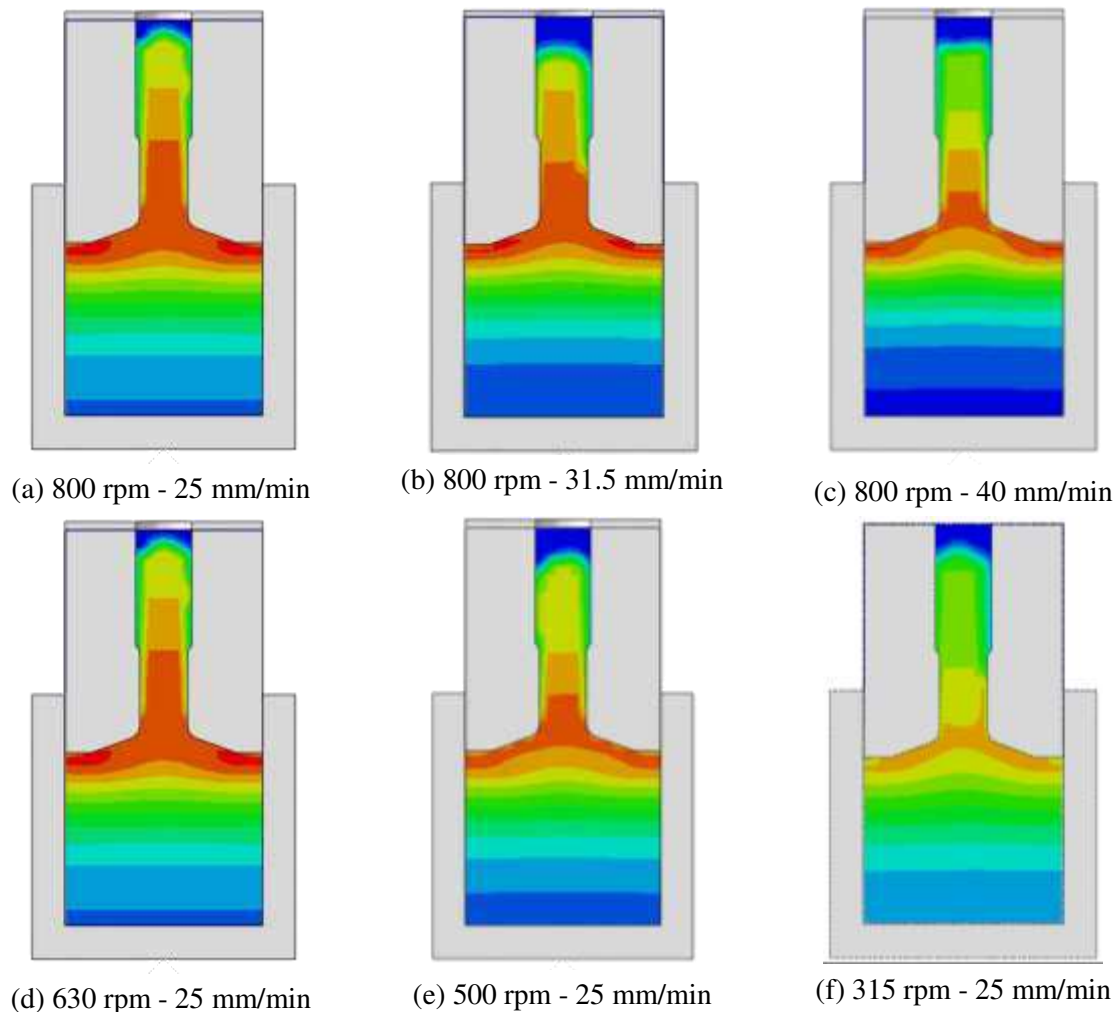

(a) 800 rpm - 25 mm/min   (b) 800 rpm - 31.5 mm/min   (c) 800 rpm - 40 mm/min

(d) 630 rpm - 25 mm/min   (e) 500 rpm - 25 mm/min   (f) 315 rpm - 25 mm/min

Fig. 6 Temperature distribution in the samples produced with different rotational and plunging speeds.

The temperature variation curves along the horizontal straight line which crosses over from the tool edges are shown in Fig. 7. As can be seen in the figure, in each individual curve the highest temperature emerges in the workpiece/tool contact point, and going toward the sample center the temperature declines. By comparing the maximum temperature achieved in different process parameters, it can be deduced that the samples with higher rotational speed to plunging speed ratio (ω/v) shows a higher maximum temperature. Additionally, it is clear that the difference between maximum temperature at the outer point of the workpiece and minimum temperature at the center of workpiece becomes deeper at higher plunging speeds. On the other words, the depth of bowl-shape curve is deeper at the higher plunging speeds and thus, it generates higher temperature gradient inside the workpiece.
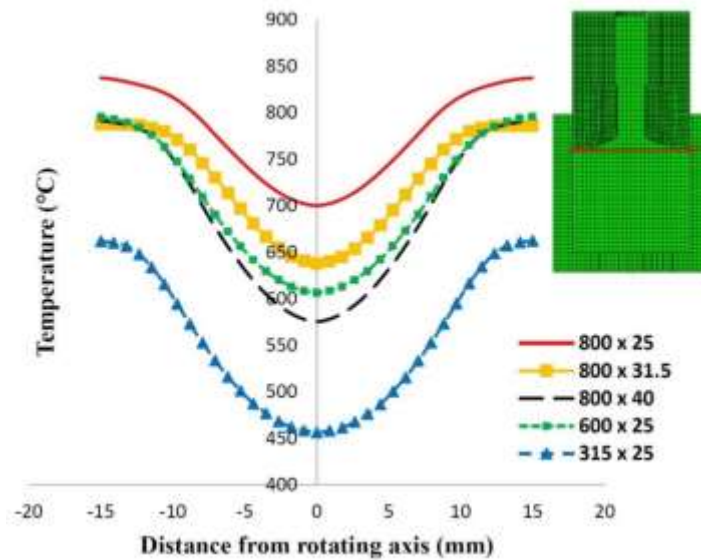

Fig. 7. Temperature variation curves along the horizontal straight line which crosses over from the tool edges (the image on the right up corner).
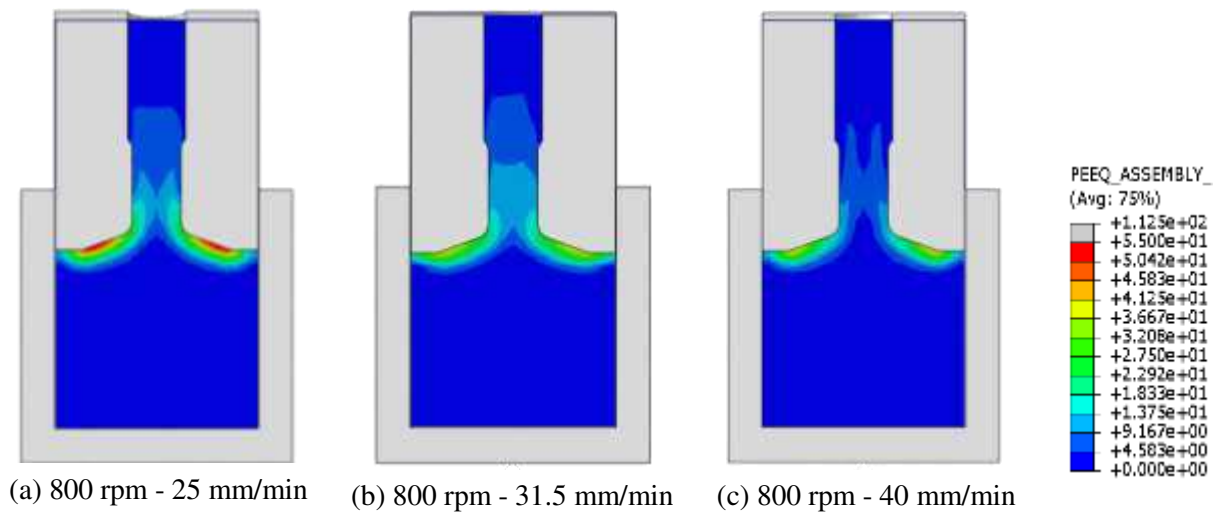
4.3. Strain distribution

Along with the thermal cycle and maximum temperature, an under process substance experiences, the plastic deformation aspects such as effective strain and strain rate, are affecting the microstructure and therefore the mechanical properties of the product. Furthermore, the amount of strain applied to the material during the friction-stir-based processes is very much higher in compare to the other severe plastic deformation (SPD) processes [23]. For instance, the maximum amount of strain can be applied by the different types of the extrusion, equal channel angular process (ECAP), and incremental forming (IF) processes is 1-5 [24]. While, it is varying between 50-200 in the FSW process, based on the tool geometry and process parameters [25]–[27]. Therefore, study on the strain is one of the key roles on considering and

determining the microstructural properties of the produced materials by FSBE. Fig. 8 describes the effects of the rotational and plunging speeds on the strain distribution. As it was expected, in all of the samples the maximum strain occurs in the tool/workpiece interface and is the highest near the outer edge of tool. Indeed, going far from the tool center increases the sweeping capability of tool which boosts both the frictional heat and plastic deformation, and these two results invigorate each other. Because, the higher the temperature, the softer the material and thus, the easier the material movement and the higher the strain.

Comparing Figs. 8a-8c, one can be concluded that an increase in the plunging speed leads to a decrease in the amount of strain which the material under process experiences. Although by increasing the plunging speed the process force increases, the process time declines and a distinct point inside the material experiences the deformation in lower amount and lower time. At the constant rotational speed of 800 rpm, when the plunging speed goes up from 25 to 40 mm/min, the strain decreases from 55 to 38 mm/mm.

In terms of the rotational speed, it is clear that a decrease in rotational speed results in a lower strain. As the strain amount from 55 mm/mm at the rotational speed of 800 rpm drops down to 35 mm/mm at the rotational speed of 315 rpm. Consequently, a lower ω/v results in a lower strain, because, a distinct point inside the material experiences lower plastic deformation over the process.

(a) 800 rpm - 25 mm/min   (b) 800 rpm - 31.5 mm/min   (c) 800 rpm - 40 mm/min

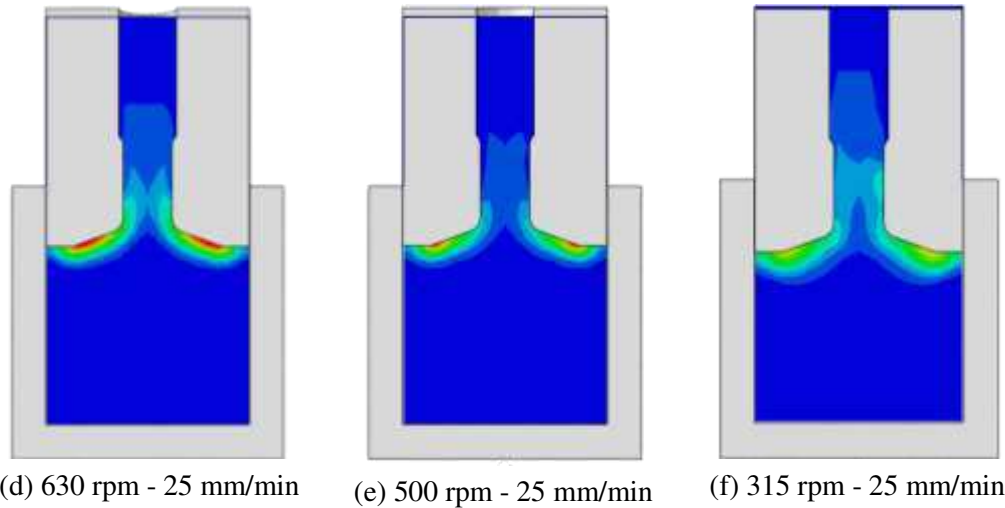(d) 630 rpm - 25 mm/min   (e) 500 rpm - 25 mm/min   (f) 315 rpm - 25 mm/min

Fig. 8 Strain distribution in the samples produced with different rotational and plunging speeds.

4.4. Microstructures

Fig. 9 shows the microstructure of base metal and the produced samples at different rotational and plunging speeds. Fig. 9a illustrates the microstructure of base metal used in this study with the grain size of almost 18.5 µm. Regarding the produced wires by FSBE, since the center and periphery of the produced wires experience different amounts of strain and temperature, the microstructure images are shown at the center and periphery of wires. Fig. 9b shows the locations on the cross section of a wire from which the microstructure images are taken. Different affecting factors can determine the grain size at the resulted microstructure. The amount of strain and the temperature history are the most affecting factors on the microstructure of FSBE samples. The higher strain will result in a higher dislocation density and more preferential sites for grain nucleation and consequently will produce a microstructure with finer grains [28]–[30]. As cited before, the amount of produced strain in the FSBE process is very high and therefore, it is expected to generate a microstructure with ultrafine grains. However, as can be seen in Fig. 9 there is no big difference between grain size of base metal and those of the produced FSBE samples. While the grain size in the base metal is almost 18.5 µm, it is varying between 10-30 µm in the produced samples by FSBE.

Besides the strain value, the temperature, that the materials are undergone during the FSBE, is more higher comparing with the other SPD processes. While the cold extrusion, ECAP and IF processes are normally applied at the ambient temperature (or a bit higher), in the FSBE process the temperature sometimes rises up to 95% of material melting point. These very high temperatures could severely diminish the effects of strain on the microstructure by growing the grains, even if several continuous dynamic recrystallizations are occurred.
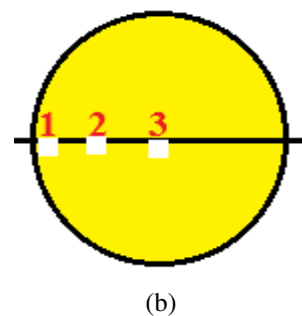
Fig. 9c shows the microstructures of the produced brass wire, using FSBE by the rotational and plunging speeds of 800 rpm and 25 mm/min, at the sample center and periphery. As can be seen the grain size at the center is 28.3 µm, while it is 27 µm at the sample periphery. The materials at the periphery of wire are mostly come from the outer layers of initial stock (will be discussed later) and in compare to the materials at the center experience higher strain. Therefore, from the strain point of view, the grains at the periphery of sample should be finer than the center. In terms of temperature, although the material at the periphery has experienced a bit higher temperature, it is almost uniform when the materials are crossing from the sizing channel (the central hole of 7 mm dia.). Additionally, when the wire passed this channel, the periphery temperature could be lower due to the thermal conduction. Consequently, it seems that the strain is the dominant factor for the microstructural deviation in the sample cross section rather than the temperature.

The effect of plunging speed on the microstructure and grain size is shown in Figs. 9c-9e and 10a. By increasing the plunging speed from 25 to 40 mm/min, although the strain amount applied to the materials is decreased (Fig. 8), it seems that 90 °C temperature drop is more effective than the strain decrease as the grain size is reduced almost 8 and 10 µm at the center and periphery of the samples, respectively. Also, along with the temperature reduction, by increasing the plunging speed the time that the material endures the higher temperatures reduces, which helps to grain growth prevention.

Figs. 9c, 9f-9h and 10b shows the effect of rotational speed on the microstructure and grain size at the center and periphery of FSBE samples. It can be seen that the grain size is reduced from 28.3 to 12.21 µm (for the samples center) by decreasing the rotational speed from 800 to 315 rpm. Similar to the plunging speed, the temperature is the dominant factor rather than the strain that the material experiences over the FSBE process.
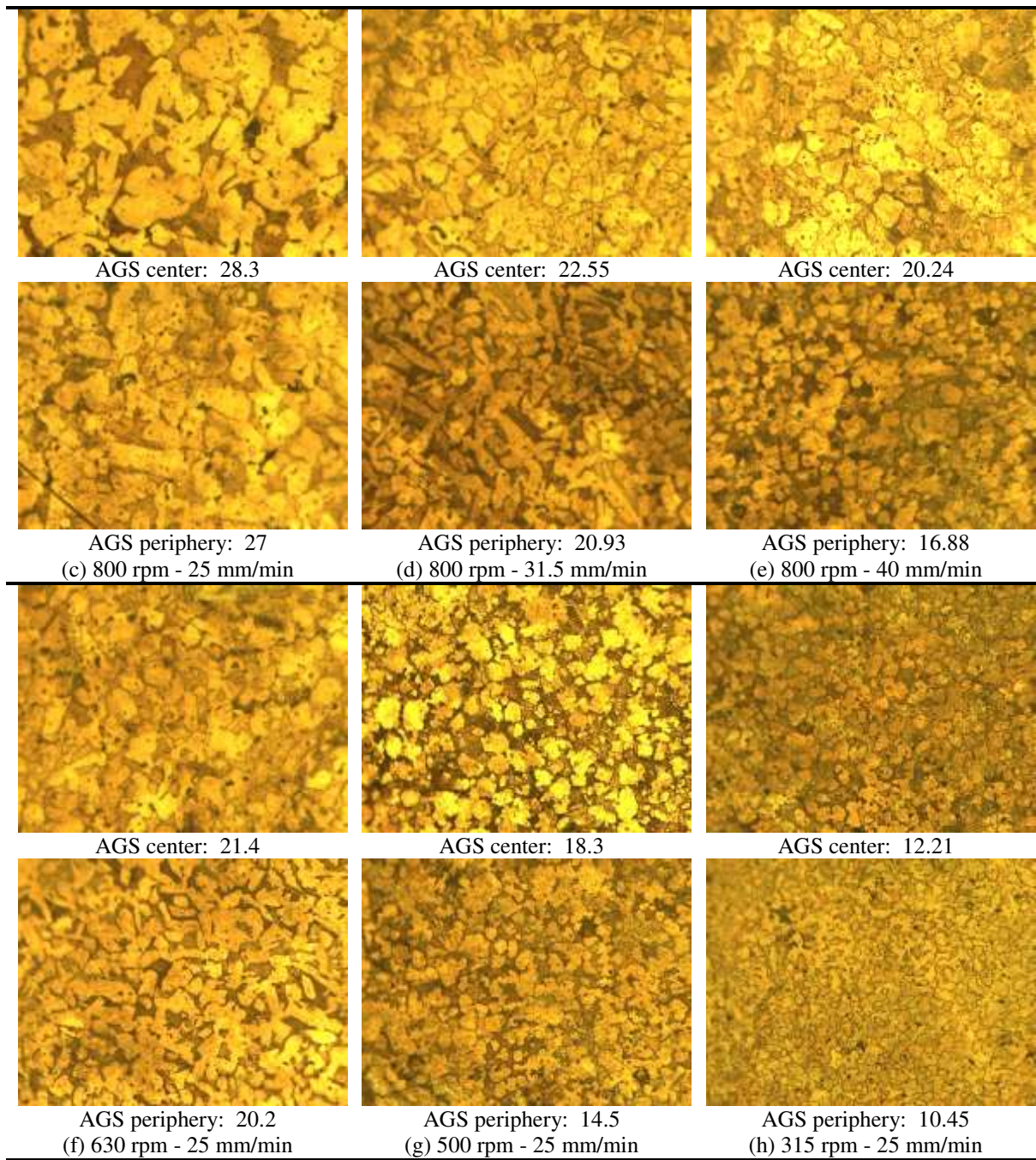

(a) AGS base metal: 18.5

(b)

AGS center: 28.3	AGS center: 22.55	AGS center: 20.24
AGS periphery: 27	AGS periphery: 20.93	AGS periphery: 16.88
(c) 800 rpm - 25 mm/min	(d) 800 rpm - 31.5 mm/min	(e) 800 rpm - 40 mm/min
AGS center: 21.4	AGS center: 18.3	AGS center: 12.21
AGS periphery: 20.2	AGS periphery: 14.5	AGS periphery: 10.45
(f) 630 rpm - 25 mm/min	(g) 500 rpm - 25 mm/min	(h) 315 rpm - 25 mm/min

Fig. 9 Microstructures in the samples produced with different rotational and plunging speeds. For each sample the upper and lower images show the microstructure of produced wire at the center and periphery, respectively. AGS is average grain size.

Generally, it can be concluded that:

(1) when the process parameters are constant (means in a sample) the microstructural deviation at the sample cross section is mostly affected by the strain. However,

(2) when the processes parameters are changed (means from one sample to the other) the temperature is the dominant factor in grain size determining.

Furthermore, paying attention to Figs. 10a and 10b, it can be deduced that at the lower ω/v ratios the difference between the center and periphery grain size becomes more tangible. It

seems that at the higher ω/v ratios, along with the rising the peak temperature, the effect of strain on the cross-section microstructural deviation becomes weaken.
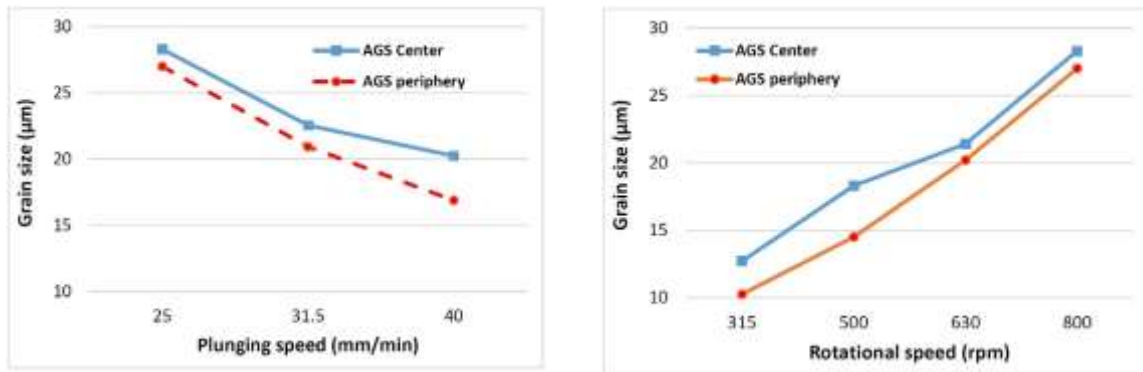

Fig. 10 Grain size variation at the center and periphery of the samples produced by FSBE. (a) Effect of plunging speed, and (b) Effect of rotational speed.

4.5. Material Flow

The developed numerical model is capable to consider the material flow during the FSBE process of brass. The point tracking technic of the ABAQUS software is used to study the material movement as well as the effects of process parameters on this movement.

(a)
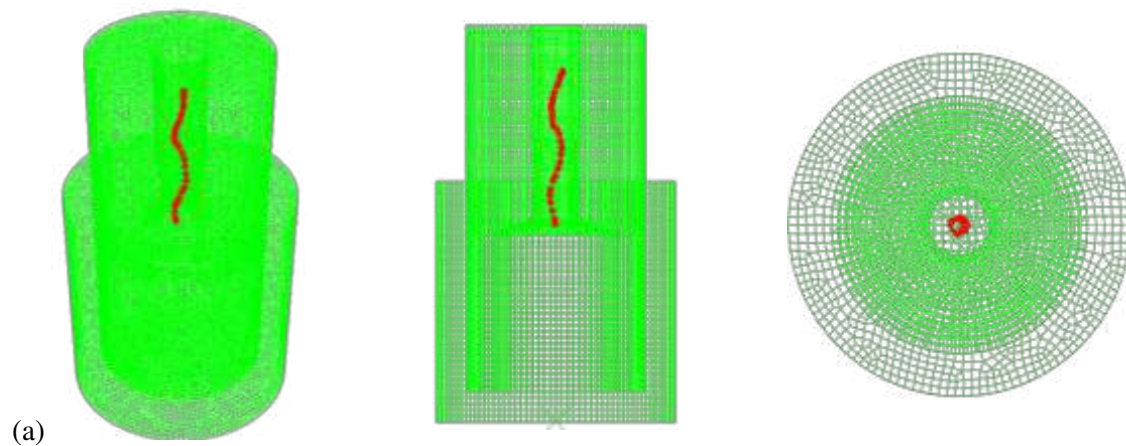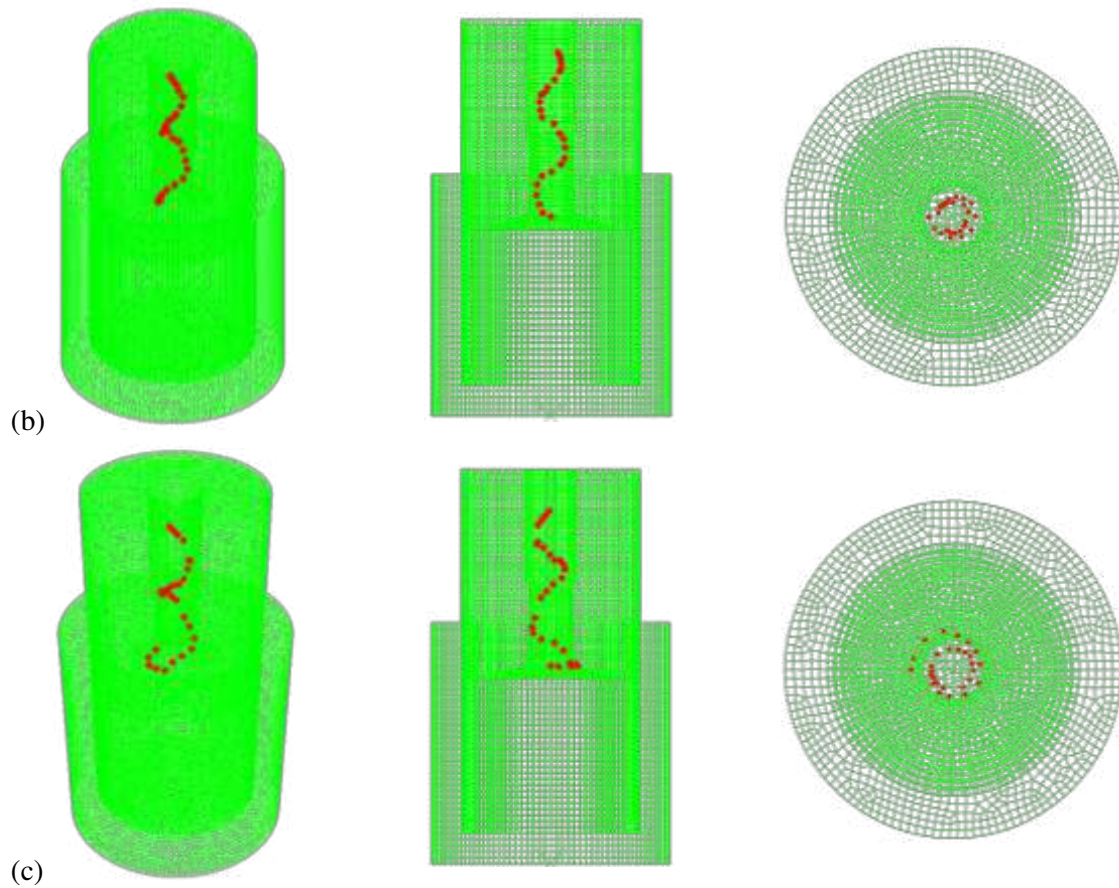
Fig. 11 The moving path during the FSBE of brass for the points at (a)1 mm, (b) 3 mm, and (c) 5 mm distance from the central axis.

To study the material flow pattern over the FSBE process, the moving paths of 3 different points located at different distances from tool axis are taken into consideration. In Figs. 11a-c the points are located at 1, 3 and 5 mm from the central axis in the initial stock. Then, their paths over the process from initial stock to final wire sample are observed from 3D, front, and top views. As can be seen all points rotate around the axis and go up in an almost helical path from the initial stock into the sizing channel to produce the wire. However, the path for the point at 1 mm distance from the center is almost pure helical and moves almost upward with a lower speed. While, for the point at 5 mm distance from center, the path is conical helix and besides the upward movement, takes an inward spiral movement and thus, it has to take longer path with higher speed. Therefore, as discussed before, a higher strain is applied to the points at higher distance from tool axis.

To consider the total material flow pattern accompanied with the effects of process parameters, different points in consecutive distances of 1.15 mm are located along the diameter of initial stock. The initial position of the points is shown in Fig. 12 from the top and front views. Then, the position of these points during the process is observed at different time intervals.
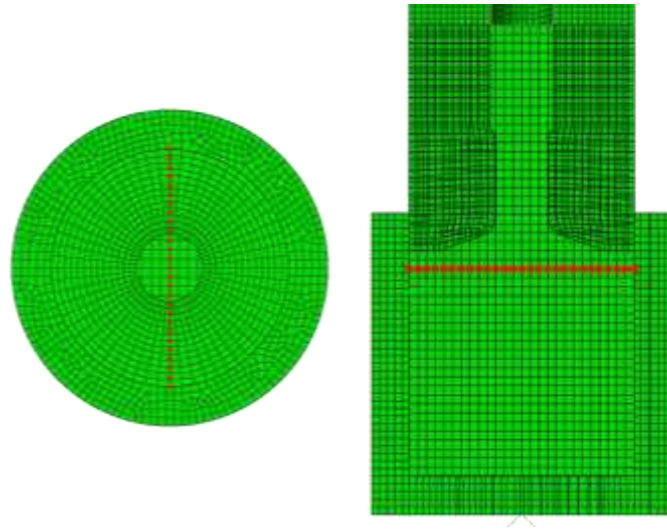
Fig. 12 Initial positions of the located points along the diameter of initial stock for material flow pattern consideration.

The effects of process parameters on the material flow pattern are shown in Figs. 13 and 14 from the top and front views. The general shape of material flow patterns in all samples are similar to each other and includes a conical helix pattern, but the speed of flowing points changes with changing the process parameters. As can be seen by increasing the plunging speed from 25 to 40 mm/min (Figs. 13a and 13b) the speed of material penetration from initial stock into the final wire increases. Furthermore, comparing the top views for two samples, one can be deduced that by increasing the plunging speed the flowing points are rotated faster. Although a reverse result was expected, it seems that when the plunging speed is increased, the points are gone faster toward the wire channel and consequently are entered faster to the deforming zone.
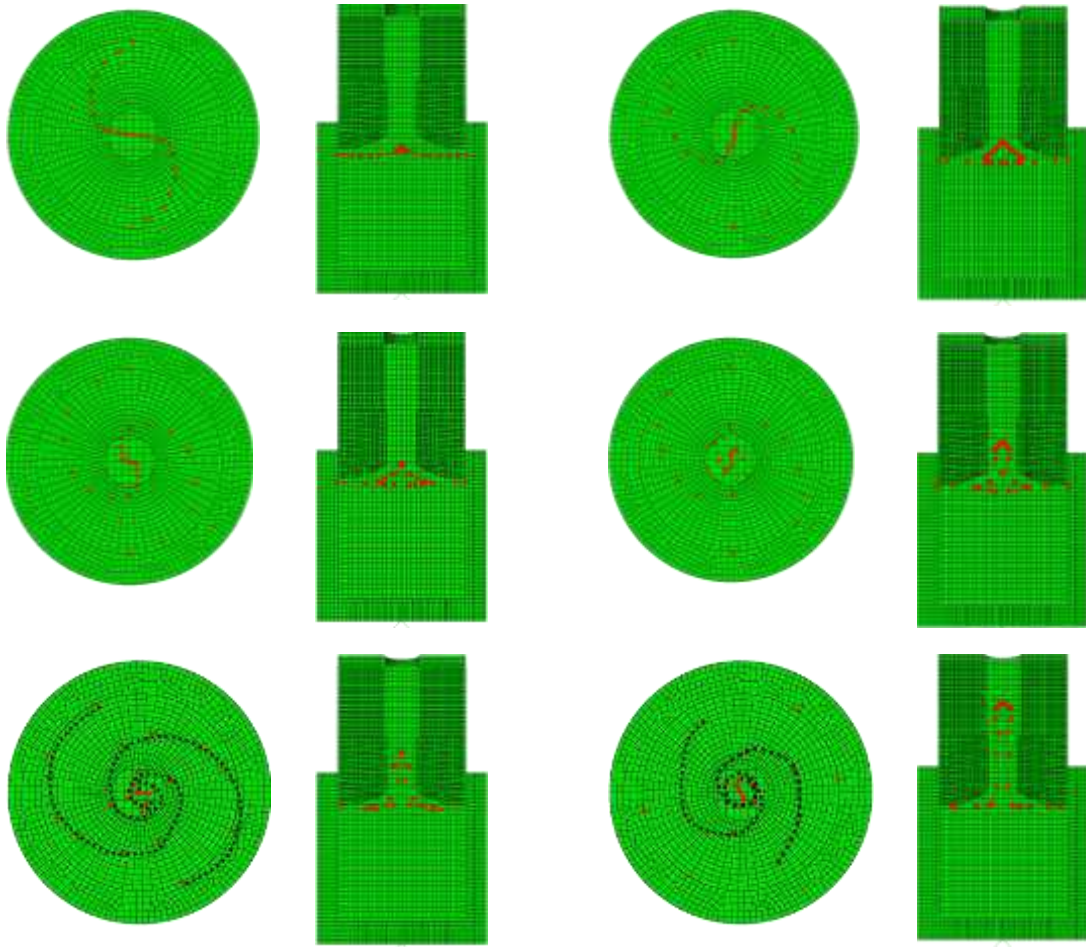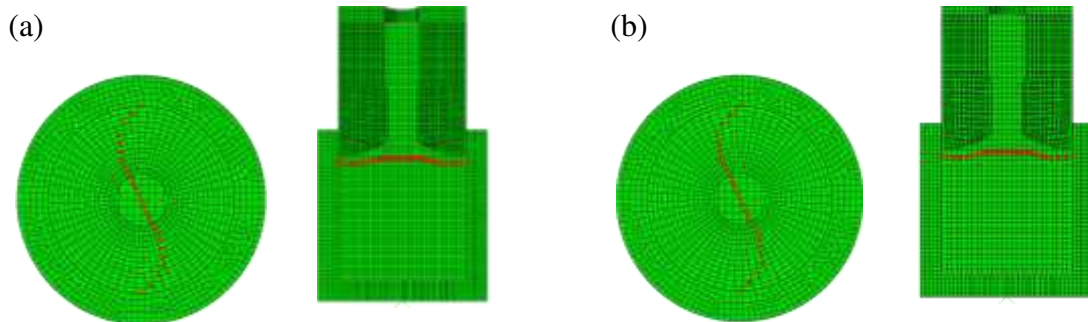
(a)

(b)
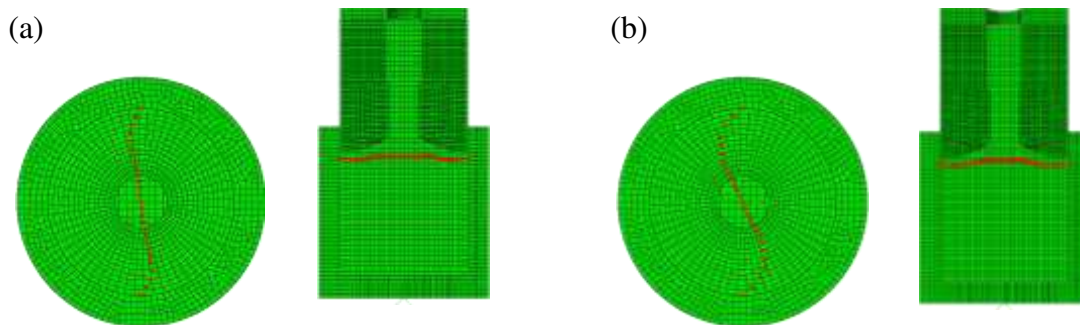
Fig. 13. The material flow pattern from top and front views at different time intervals. (a) 800 rpm and 25 mm/min, and (b) 800 rpm and 40 mm/min.

Similar effect can be observed when the rotational speed is reduced from 800 to 500 rpm (comparing Figs. 14a, and 14b). Actually in this case, the number of rotations for a point lowers before entering to the sizing channel. Therefore, although the speed of entering the points from initial channel into the sizing channel is the same (comparing the front views for 2 samples in Fig. 14), the number of rotations before entering to the channel is reduced by decreasing the rotational speed from 800 to 500 rpm. This will lead the materials to experience lower strain over the FSBE process.
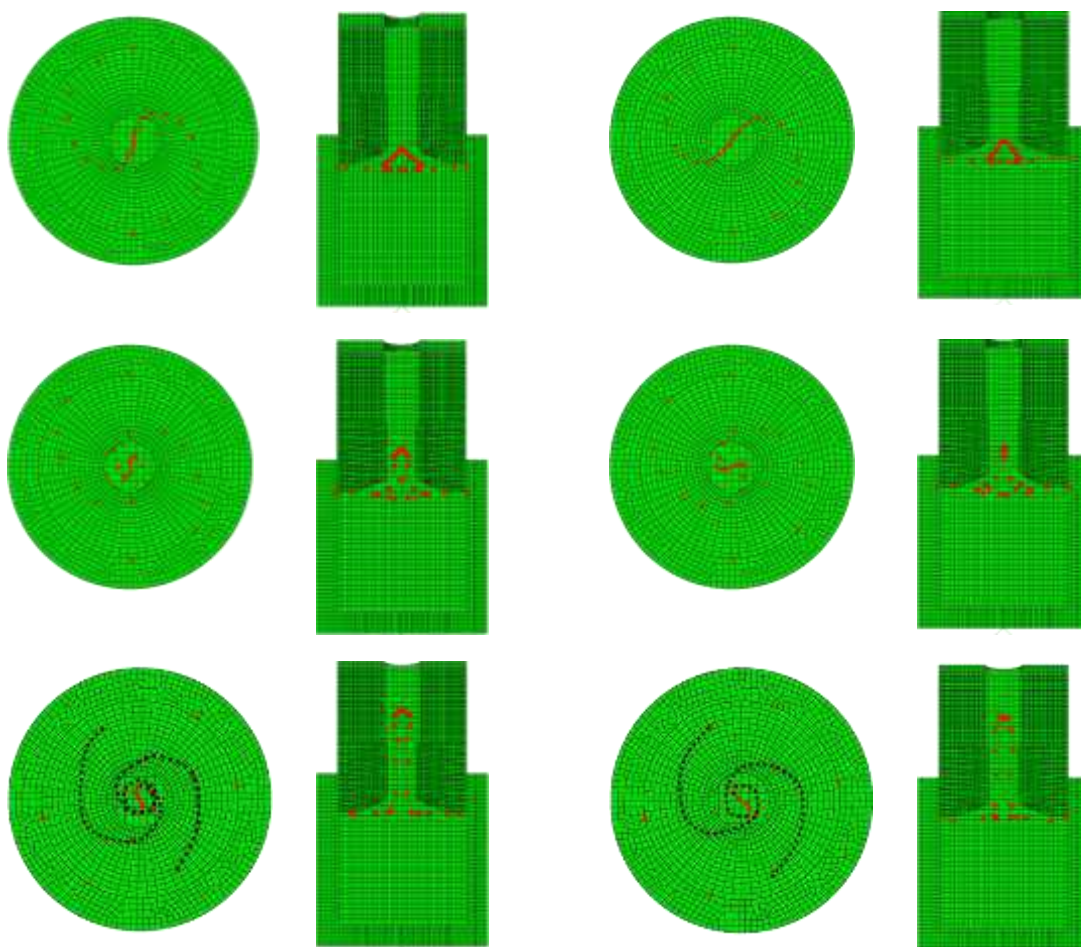
(a)　　　　　　　　　　　　　　　(b)

Fig. 14. The material flow pattern from top and front views at different time intervals. (a) 800 rpm and 40 mm/min, and (b) 500 rpm and 40 mm/min.

5. Conclusions

In the present work, a primary 30-mm diameter brass shaft (as the initial stock) is formed to the 7-mm brass wire using friction stir back extrusion process. Additionally, a 3D Coupled Eulerian Lagrangian model developed using the ABAQUS software to simulate the FSBE process of brass and verified by experiments. Then, the effects of process parameters of tool rotational and plunging speed on the temperature and strain distributions, microstructure, and material flow patterns are considered. The results show that:

- The highest temperature and strain occurs near the tool/workpiece interface but in a further distance from the tool axis. The higher rotational speed or lower plunging speed cause to an increase in the temperature and strain that the material experiences during the process.

- In the cross-section of a produced FSBE sample (wire) the microstructure is finer in the periphery rather than the center. This microstructural deviation is mostly affected by the strain rather than the temperature.

- However, when the process parameters are changed the dominant factor in determining the product microstructure is the temperature rather than the strain. Therefore, a higher rotational to plunging speed ratio will result in a coarser microstructure.

- The pattern of material flow during the FSBE process is conical helix (since the tool head is conical), and does not change significantly by the process parameters. The points at the further distance from the tool axis, along with an upward movement, experience an inward spiral movement which is amplified by higher rotational speed. However, the material very near the tool axis almost take an upward movement and endure a very lower strain.

- The plunging speed is responsible for the wire production speed while the rotational speed is responsible for the frictional heat and strain generation.

Database Availability

All of the required experimental data for reproduction of these findings is explained with details in section "2. Experimental procedure".

The general data for reproduction of proposed simulation model is described in section "3. Simulation model"; however, some negligible details cannot be shared at this time as the data also forms part of an ongoing study.

Authors' contributions

All authors have participated in conception, design, analysis, and interpretation of the data as well as the writing, drafting and revising the article.

Ethical approval

Since the study is performed on the metallic samples, there is no need for ethical approval; however, all the tests are done in Imam Khomeini International University, in the metal forming, material processing, and SEM and XRD Labs under the control of trained experts. Additionally, the paper main data is not published elsewhere.

Consent to participate

All authors declare that have agreed for authorship, have read and approved the manuscript, and have given the consent for submission and subsequent publication of the manuscript.

Competing interests

The authors declare that they have no competing of interest

References

[1]   A. Heidarzadeh, "Tensile behavior, microstructure, and substructure of the friction stir welded 70/30 brass joints: RSM, EBSD, and TEM study," *Arch. Civ. Mech. Eng.*, vol. 19, no. 1, pp. 137–146, 2019.

[2]   E. E. Igelegbai, O. A. Alo, A. O. Adeodu, and I. A. Daniyan, "Evaluation of Mechanical and Microstructural Properties of <i>α</i>-Brass Alloy Produced from Scrap Copper and Zinc Metal through Sand Casting Process," *J. Miner. Mater. Charact. Eng.*, vol. 05, no. 01, pp. 18–28, 2017.

[3]   A. Heidarzadeh, H. M. Laleh, H. Gerami, P. Hosseinpour, M. J. Shabestari, and R. Bahari, "The origin of different microstructural and strengthening mechanisms of copper and brass in their dissimilar friction stir welded joint," *Mater. Sci. Eng. A*, vol. 735, no. May, pp. 336–342, 2018.

[4]   A. Heidarzadeh, R. V. Barenji, V. Khalili, and G. Güleryüz, "Optimizing the friction stir welding of the α/β brass plates to obtain the highest strength and elongation," *Vacuum*, vol. 159, pp. 152–160, 2019.

[5]   M. Galai *et al.*, "α-Brass and (α + β) Brass Degradation Processes in Azrou Soil Medium Used in Plumbing Devices," *J. Bio- Tribo-Corrosion*, vol. 3, no. 3, 2017.

[6]   Q. Zhai Advisor and C. Yuan, "Recycling Metal Chips from Manufacturing Industry through a Combined Hydrodynamic and Electromagnetic Separation Approach Student Project Report," no. May, 2012.

[7]   H. B. Karadag, T. Bahtli, and M. Kara, "The Recycling of Steel and Brass Chips to Produce Composite Materials via Cold Pressing and Sintering," *Int. J. Eng. Sci.*, vol. 5, no. 5, pp. 1–6, 2016.

[8]   G. Güleryüz, "Relationship between FSW parameters and hardness of the ferritic steel joints: Modeling and optimization," *Vacuum*, vol. 178, p. 109449, Aug. 2020.

[9]   A. Yazdipour and A. Heidarzadeh, "Effect of friction stir welding on microstructure and mechanical properties of dissimilar Al 5083-H321 and 316L stainless steel alloy joints," *J. Alloys Compd.*, vol. 680, pp. 595–603, 2016.

[10]   F. Abu-Farha, "A preliminary study on the feasibility of friction stir back extrusion," *Scr. Mater.*, vol. 66, no. 9, pp. 615–618, 2012.

[11]   I. Dinaharan, R. Sathiskumar, S. J. Vijay, and N. Murugan, "Microstructural Characterization of Pure Copper Tubes Produced by a Novel Method Friction Stir Back Extrusion," *Procedia Mater. Sci.*, vol. 5, pp. 1502–1508, 2014.

[12]   N. Mathew, I. Dinaharan, S. J. Vijay, and N. Murugan, "Microstructure and Mechanical Characterization of Aluminum Seamless Tubes Produced by Friction Stir Back Extrusion," *Trans. Indian Inst. Met.*, vol. 69, no. 10, pp. 1811–1818, 2016.

[13]   S. Zhang *et al.*, "Microstructure Evolution and Mechanical Property Characterization of 6063 Aluminum Alloy Tubes Processed with Friction Stir Back Extrusion," *Jom*, vol. 71, no. 12, pp. 4436–4444, 2019.

[14]   R. A. Behnagh *et al.*, "Experimental analysis and microstructure modeling of friction stir extrusion of magnesium chips," *J. Manuf. Sci. Eng. Trans. ASME*, vol. 138, no. 4, pp. 1–11, Oct. 2016.

[15]   D. Baffari, G. Buffa, D. Campanella, L. Fratini, and A. P. Reynolds, "Process mechanics in Friction Stir Extrusion of magnesium alloys chips through experiments and numerical simulation," *J. Manuf. Process.*, vol. 29, pp. 41–49, 2017.

[16]   D. Baffari, G. Buffa, and L. Fratini, "A numerical model for Wire integrity prediction in Friction Stir Extrusion of magnesium alloys," *J. Mater. Process. Technol.*, vol. 247, pp. 1–10, 2017.

[17]   B. Meyghani, M. B. Awang, S. S. Emamian, M. K. B. Mohd Nor, and S. R. Pedapati, "A comparison of different finite element methods in the thermal analysis of friction stir welding (FSW)," *Metals (Basel).*, vol. 7, no. 10, 2017.

[18]   M. Assidi, L. Fourment, S. Guerdoux, and T. Nelson, "Friction model for friction stir welding process simulation: Calibrations from welding experiments," *Int. J. Mach. Tools Manuf.*, vol. 50, no. 2, pp. 143–155, 2010.

[19]   M. A. Ansari, A. Samanta, R. A. Behnagh, and H. Ding, "An efficient coupled Eulerian-Lagrangian finite element model for friction stir processing," *Int. J. Adv. Manuf. Technol.*, vol. 101, no. 5–8, pp. 1495–1508, 2019.

[20]   I. Dinaharan, S. Zhang, G. Chen, and Q. Shi, "Titanium particulate reinforced AZ31 magnesium matrix composites with improved ductility prepared using friction stir processing," *Mater. Sci. Eng. A*, vol. 772, p. 138793, Jan. 2020.

[21]   I. Dinaharan, R. Thirunavukkarasu, N. Murugan, and E. T. Akinlabi, "Microstructure Evolution and Tensile Behavior of Dissimilar Friction Stir-Welded Pure Copper and Dual-Phase Brass," *Metallogr. Microstruct. Anal.*, vol. 8, no. 5, pp. 735–748, 2019.

[22]   M. Akbari, P. Asadi, M. B. Givi, and P. Zolghadr, "A cellular automaton model for microstructural simulation of friction stir welded AZ91 magnesium alloy," *Model. Simul. Mater. Sci. Eng.*, vol. 24, no. 3, 2016.

[23]   P. Asadi, M. Akbari, and H. Karimi-Nemch, *Simulation of friction stir welding and processing.* 2014.

[24]   P. Tayebi, A. Fazli, P. Asadi, and M. Soltanpour, "Formability analysis of dissimilar friction stir welded AA 6061 and AA 5083 blanks by SPIF process," *CIRP J. Manuf. Sci. Technol.*, 2019.

[25]   A. Forsström, S. Bossuyt, Y. Yagodzinskyy, K. Tsuzaki, and H. Hänninen, "Strain localization in copper canister FSW welds for spent nuclear fuel disposal," *J. Nucl. Mater.*, vol. 523, pp. 347–359, 2019.

[26]   P. Asadi, M. K. Besharati Givi, and M. Akbari, "Microstructural simulation of friction stir welding using a cellular automaton method: a microstructure prediction of AZ91 magnesium alloy," *Int. J. Mech. Mater. Eng.*, vol. 10, no. 1, p. 20, Aug. 2015.

[27]   L. Fratini, G. Buffa, and L. Lo Monaco, "Improved FE model for simulation of friction stir welding of different materials," *Sci. Technol. Weld. Join.*, vol. 15, no. 3, pp. 199–207, 2010.

[28]   A. Heidarzadeh, K. Kazemi-Choobi, H. Hanifian, and P. Asadi, *Microstructural evolution.* 2014.

[29]   G. Li *et al.*, "Effect of self-reacting friction stir welding on microstructure and mechanical properties of Mg-Al-Zn alloy joints," *J. Manuf. Process.*, vol. 37, no. July 2018, pp. 1–10, 2019.

[30]   J. Zhang *et al.*, "Optimizing the mechanical properties of friction stir welded dissimilar joint of AM60 and AZ31 alloys by controlling deformation behavior," *Mater. Sci. Eng. A*, vol. 773, 2020.

Figures

(a)

(b)

(C)

Figure 1

(a) The matrix with its dimensions, (b) the tool with its dimensions, and (c) some of the produced 7-mm-diameter wires produced by FSBE.
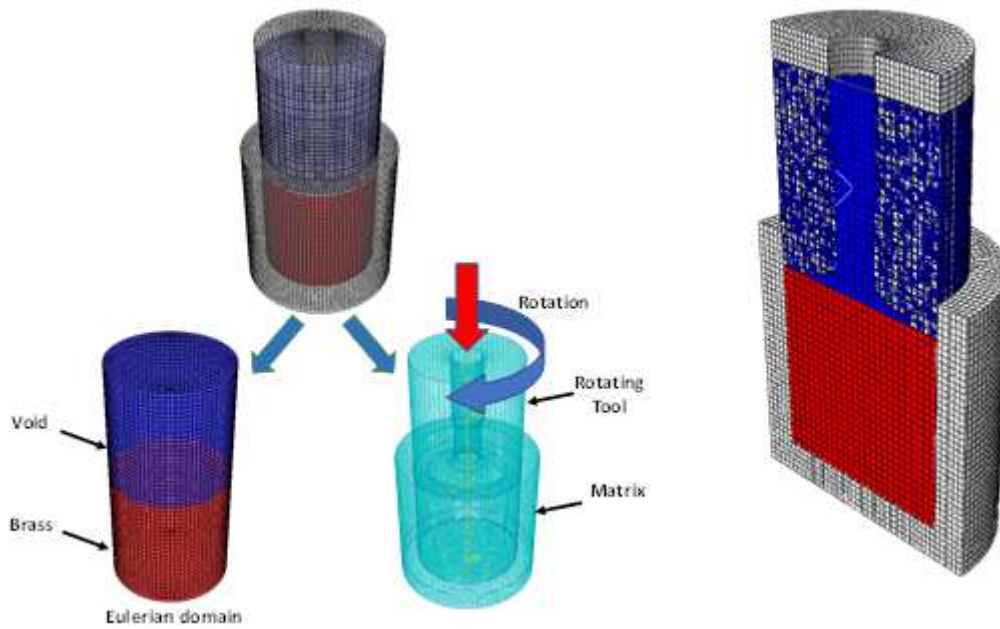
Figure 2

The material layout used in the present model for FSBE to produce the brass wires.
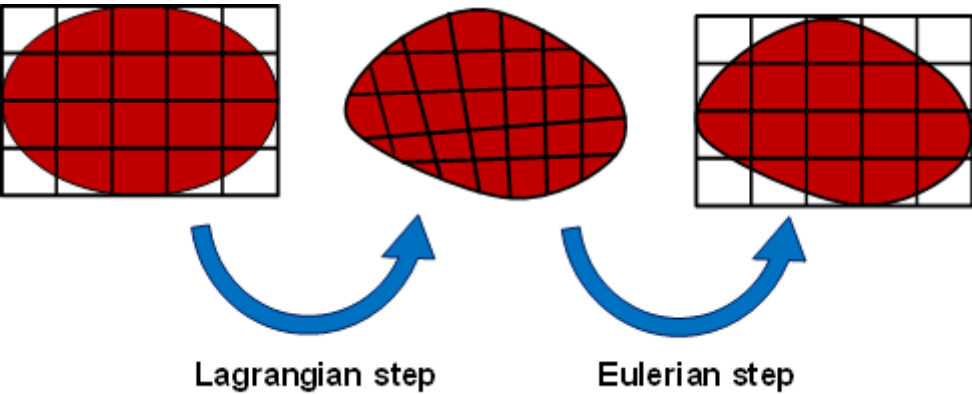

Figure 3

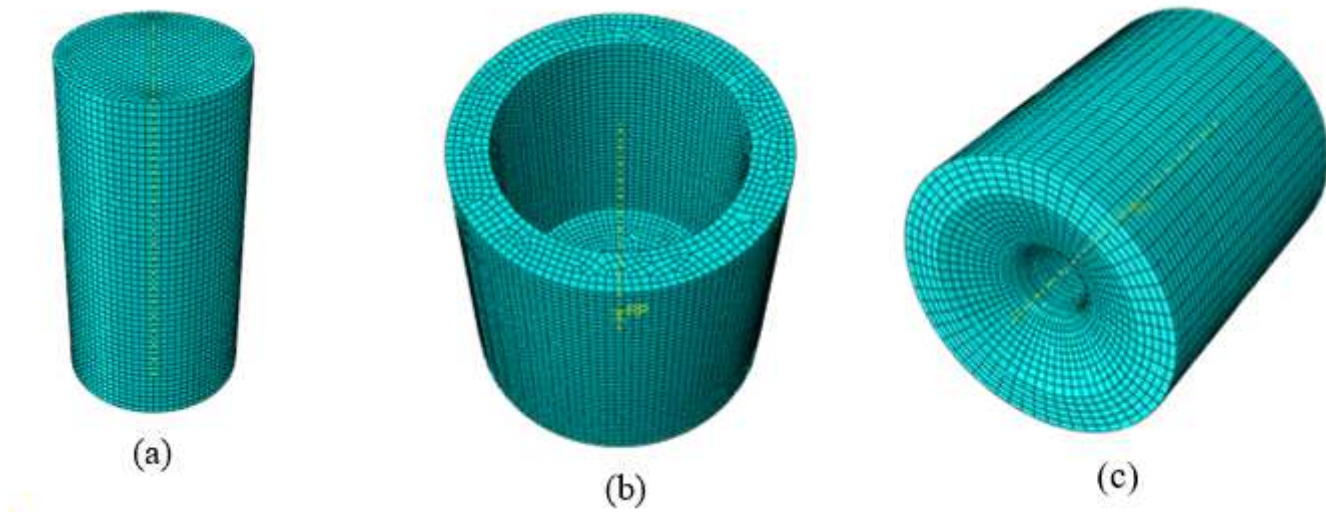Schematic illustration of the split operator in CEL method.

Figure 4

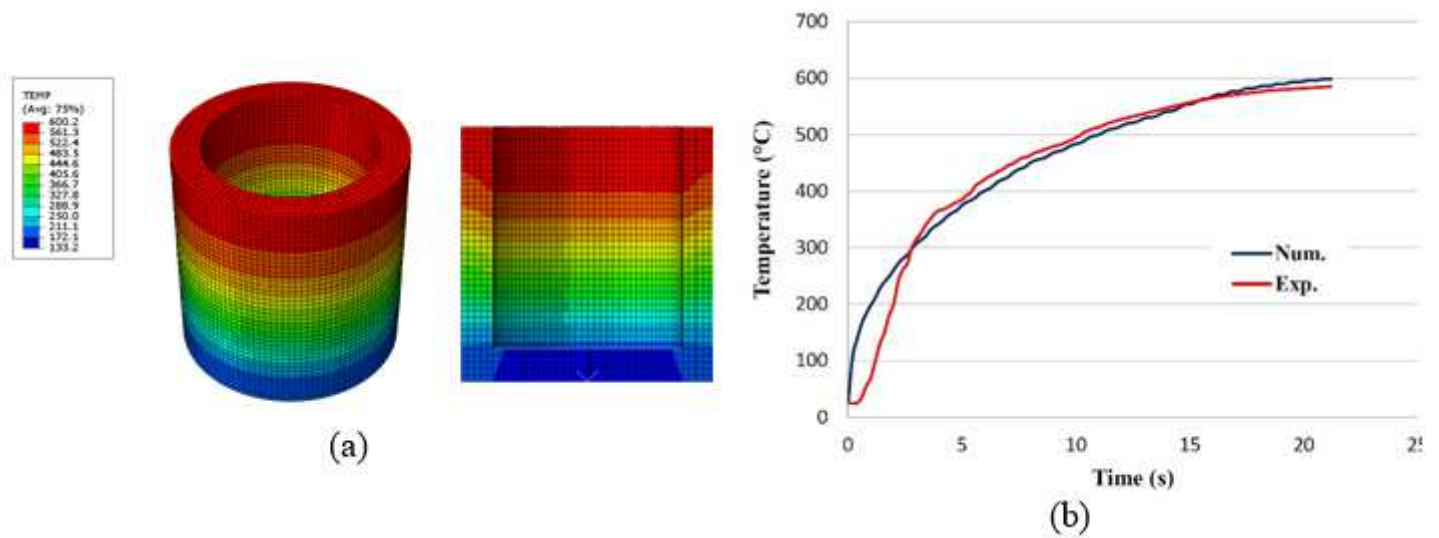Mesh in the CEL model: (a) Eulerian mesh for the workpiece, and (b) and (c) Lagrangian mesh for the tool.

Figure 5

(a) The temperature distribution in the matrix body over the FSBE process; the tool is penetrated 5 mm into the workpiece. (b) The experimental and numerical temperature history curves. The rotational and plunging speeds: 800 rpm and 25 mm/min.
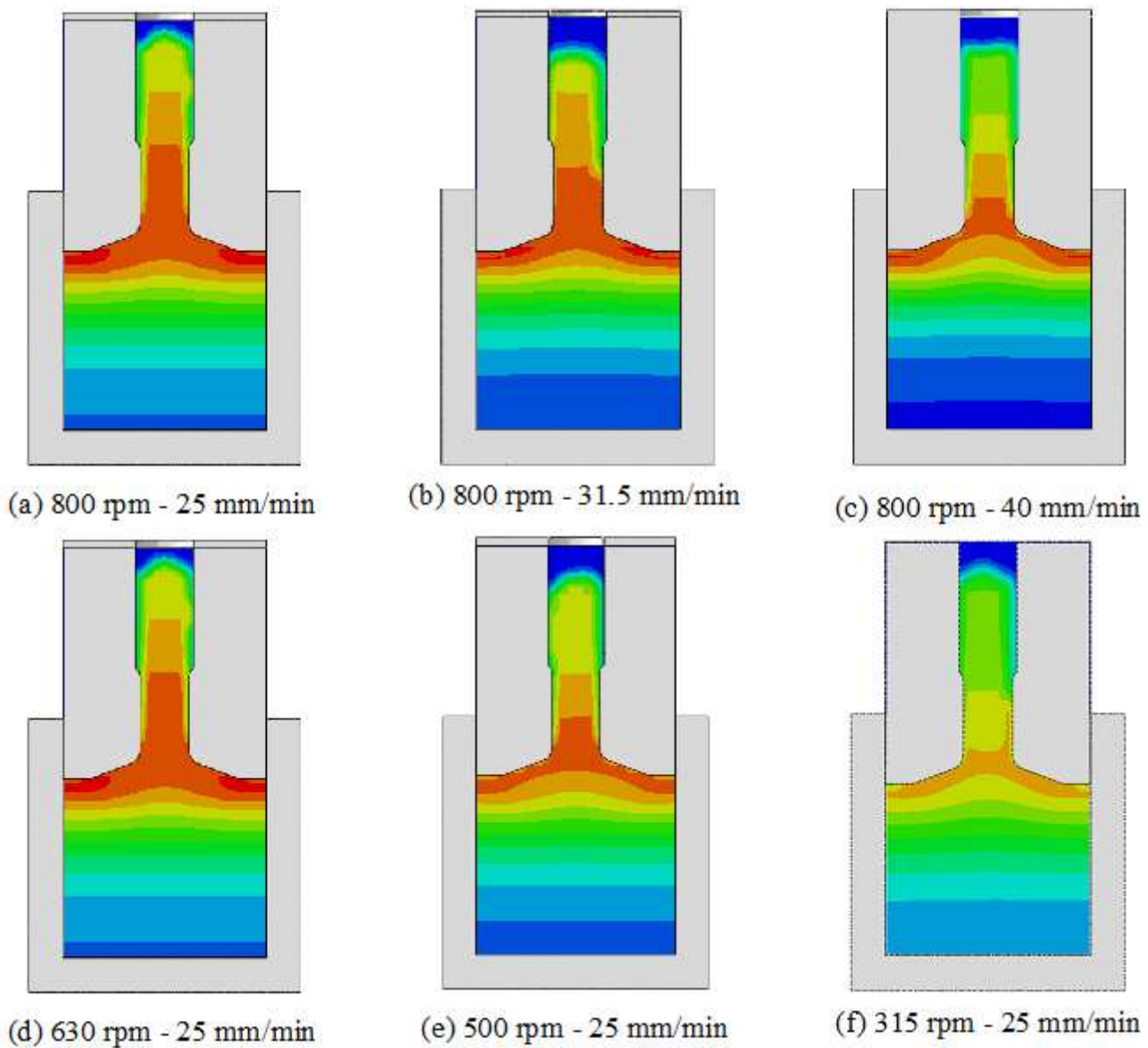
(a) 800 rpm - 25 mm/min

(b) 800 rpm - 31.5 mm/min

(c) 800 rpm - 40 mm/min

(d) 630 rpm - 25 mm/min

(e) 500 rpm - 25 mm/min

(f) 315 rpm - 25 mm/min

Figure 6

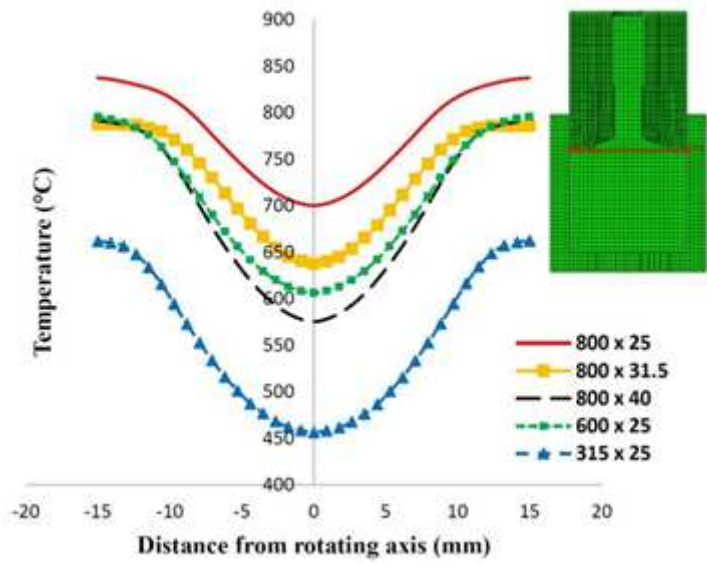Temperature distribution in the samples produced with different rotational and plunging speeds.

Figure 7

Temperature variation curves along the horizontal straight line which crosses over from the tool edges (the image on the right up corner).
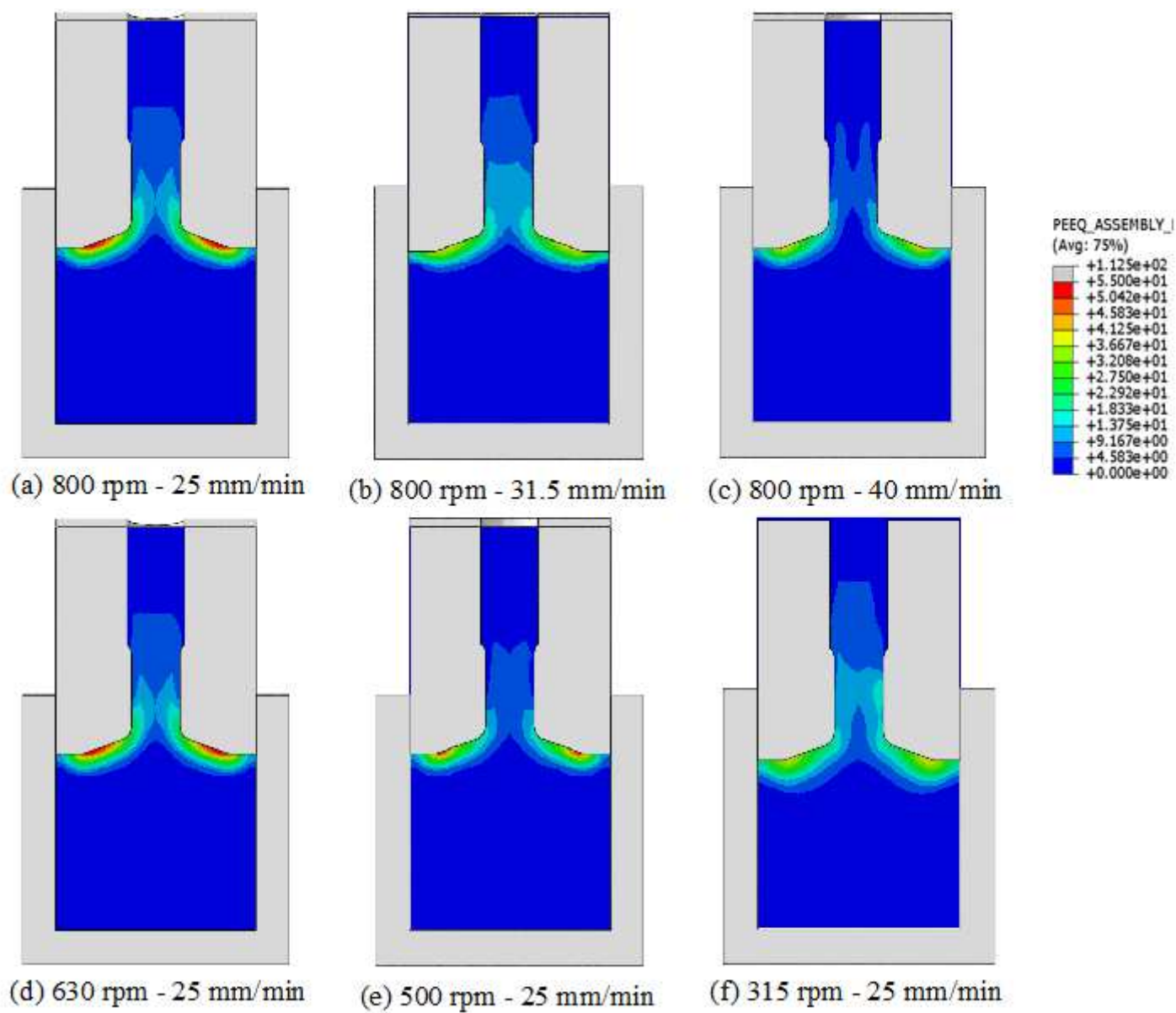
PEEQ_ASSEMBLY_
(Avg: 75%)
+1.125e+02
+5.500e+01
+5.042e+01
+4.583e+01
+4.125e+01
+3.667e+01
+3.208e+01
+2.750e+01
+2.292e+01
+1.833e+01
+1.375e+01
+9.167e+00
+4.583e+00
+0.000e+00

(a) 800 rpm - 25 mm/min (b) 800 rpm - 31.5 mm/min (c) 800 rpm - 40 mm/min

(d) 630 rpm - 25 mm/min (e) 500 rpm - 25 mm/min (f) 315 rpm - 25 mm/min

Figure 8

Strain distribution in the samples produced with different rotational and plunging speeds.

(a) AGS base metal: 18.5

(b)

AGS center: 28.3

AGS center: 22.55

AGS center: 20.24

AGS periphery: 27
(c) 800 rpm - 25 mm/min

AGS periphery: 20.93
(d) 800 rpm - 31.5 mm/min

AGS periphery: 16.88
(e) 800 rpm - 40 mm/min

AGS center: 21.4

AGS center: 18.3

AGS center: 12.21

AGS periphery: 20.2
(f) 630 rpm - 25 mm/min

AGS periphery: 14.5
(g) 500 rpm - 25 mm/min

AGS periphery: 10.45
(h) 315 rpm - 25 mm/min
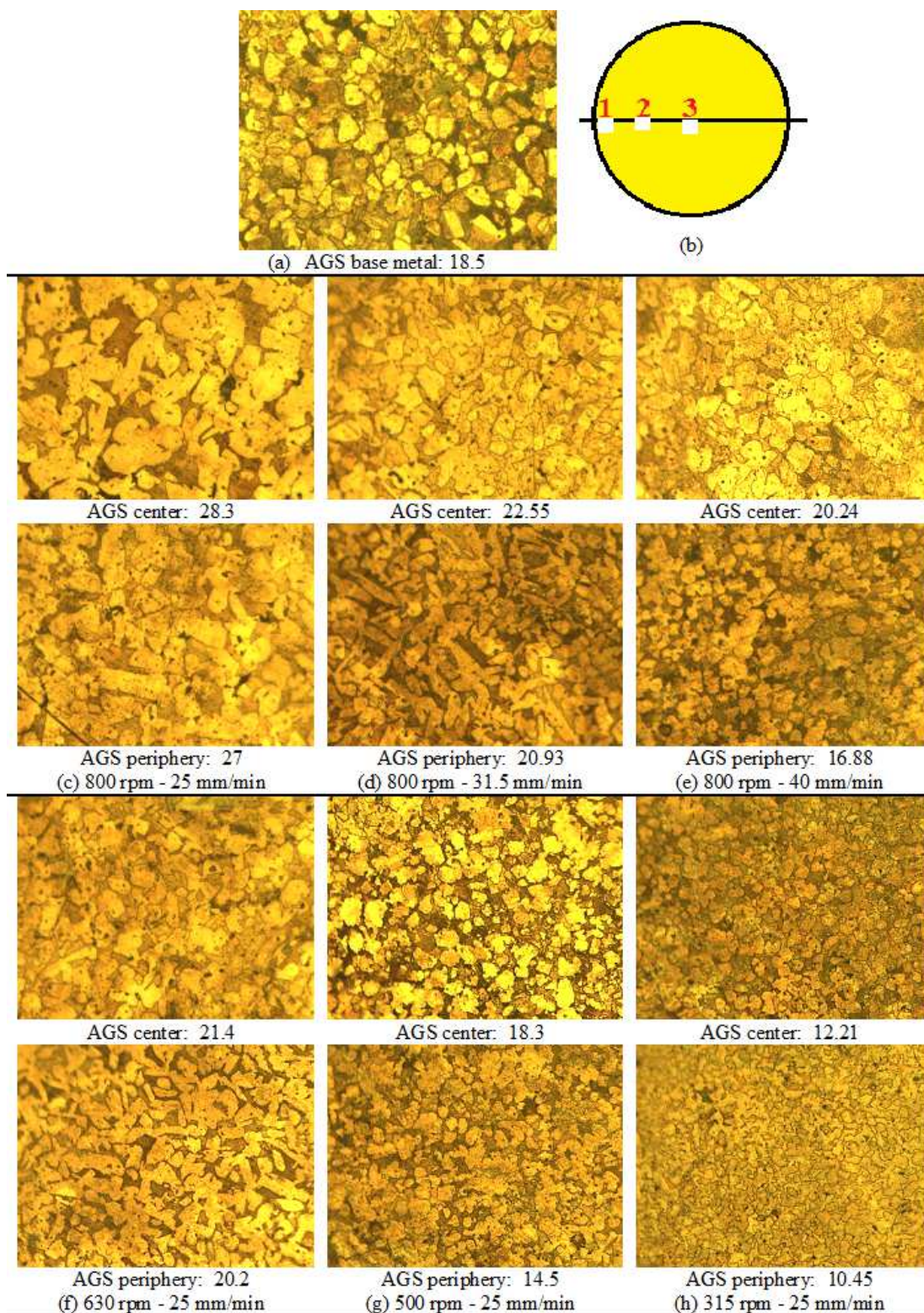
Figure 9

Microstructures in the samples produced with different rotational and plunging speeds. For each sample the upper and lower images show the microstructure of produced wire at the center and periphery, respectively. AGS is average grain size.
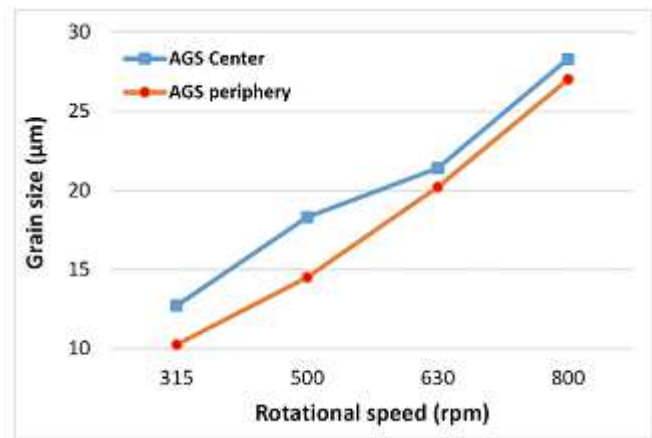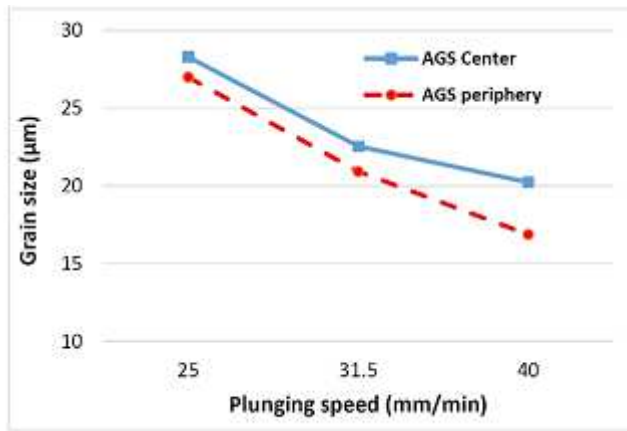
Figure 10

Grain size variation at the center and periphery of the samples produced by FSBE. (a) Effect of plunging speed, and (b) Effect of rotational speed.
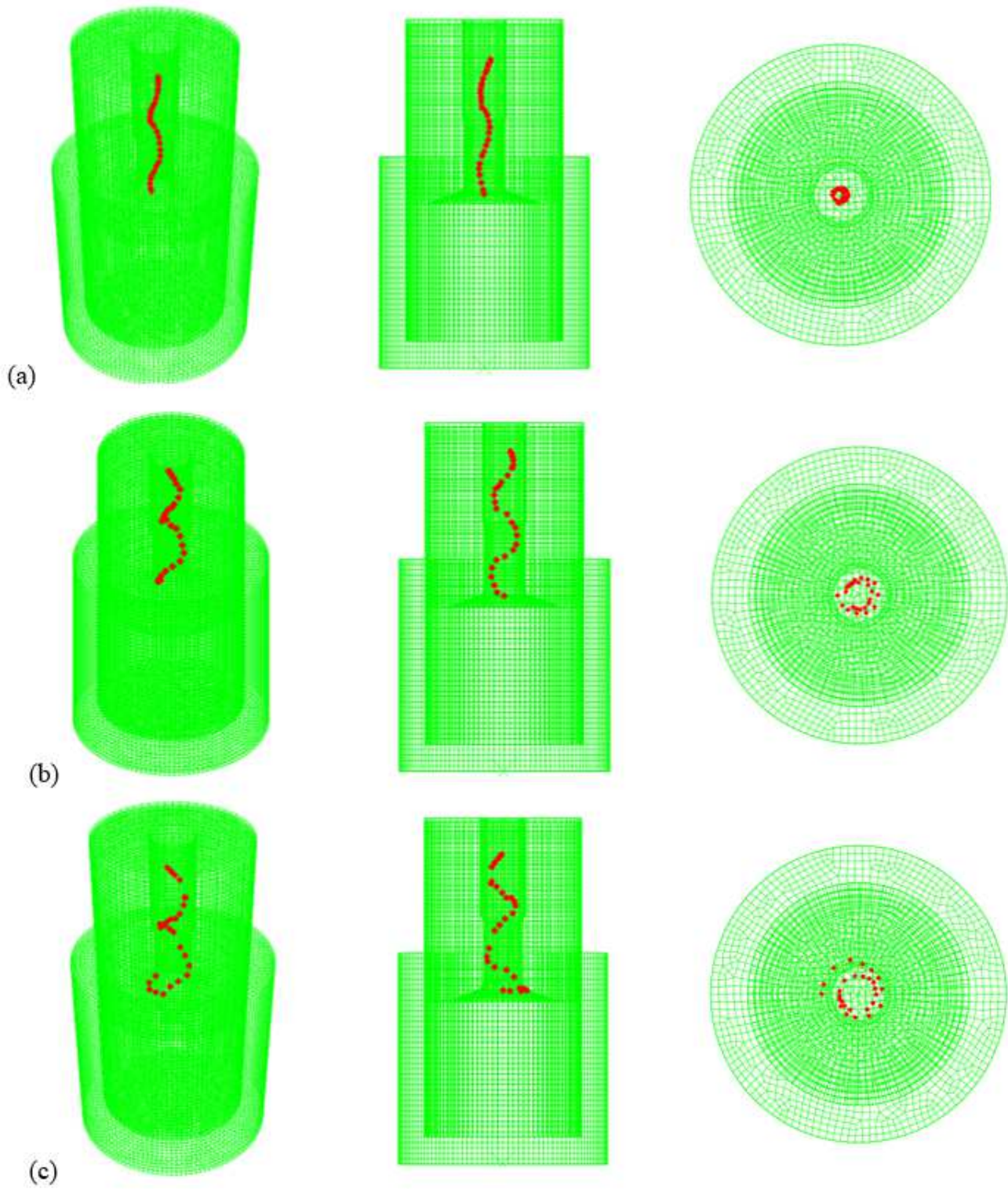
Figure 11

The moving path during the FSBE of brass for the points at (a)1 mm, (b) 3 mm, and (c) 5 mm distance from the central axis.
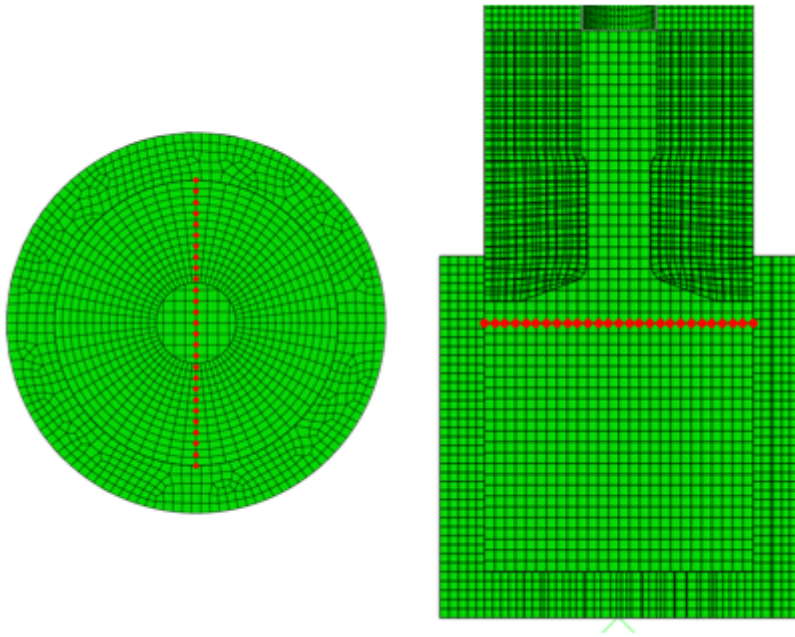
Figure 12

Initial positions of the located points along the diameter of initial stock for material flow pattern consideration.
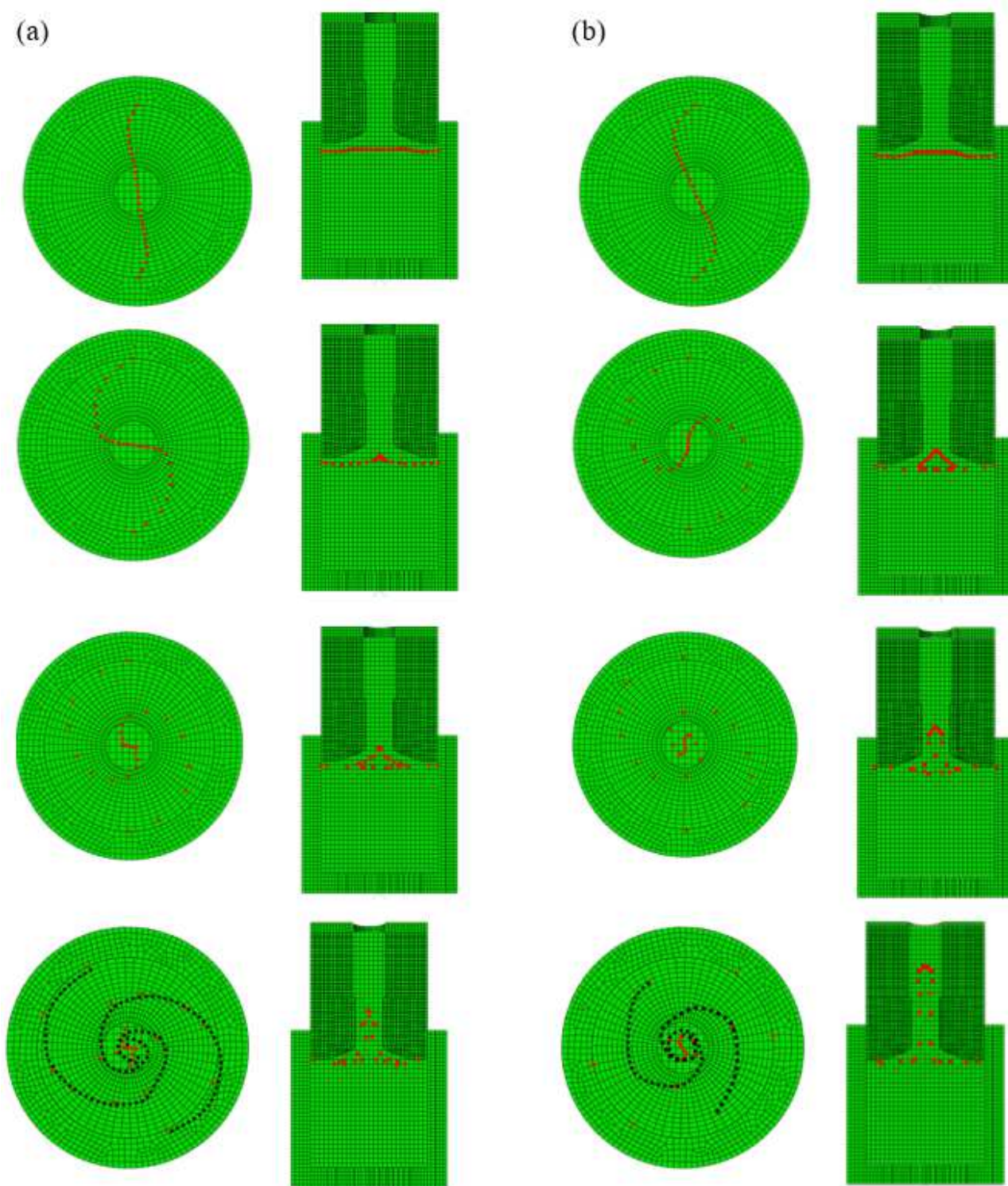
Figure 13

The material flow pattern from top and front views at different time intervals. (a) 800 rpm and 25 mm/min, and (b) 800 rpm and 40 mm/min.
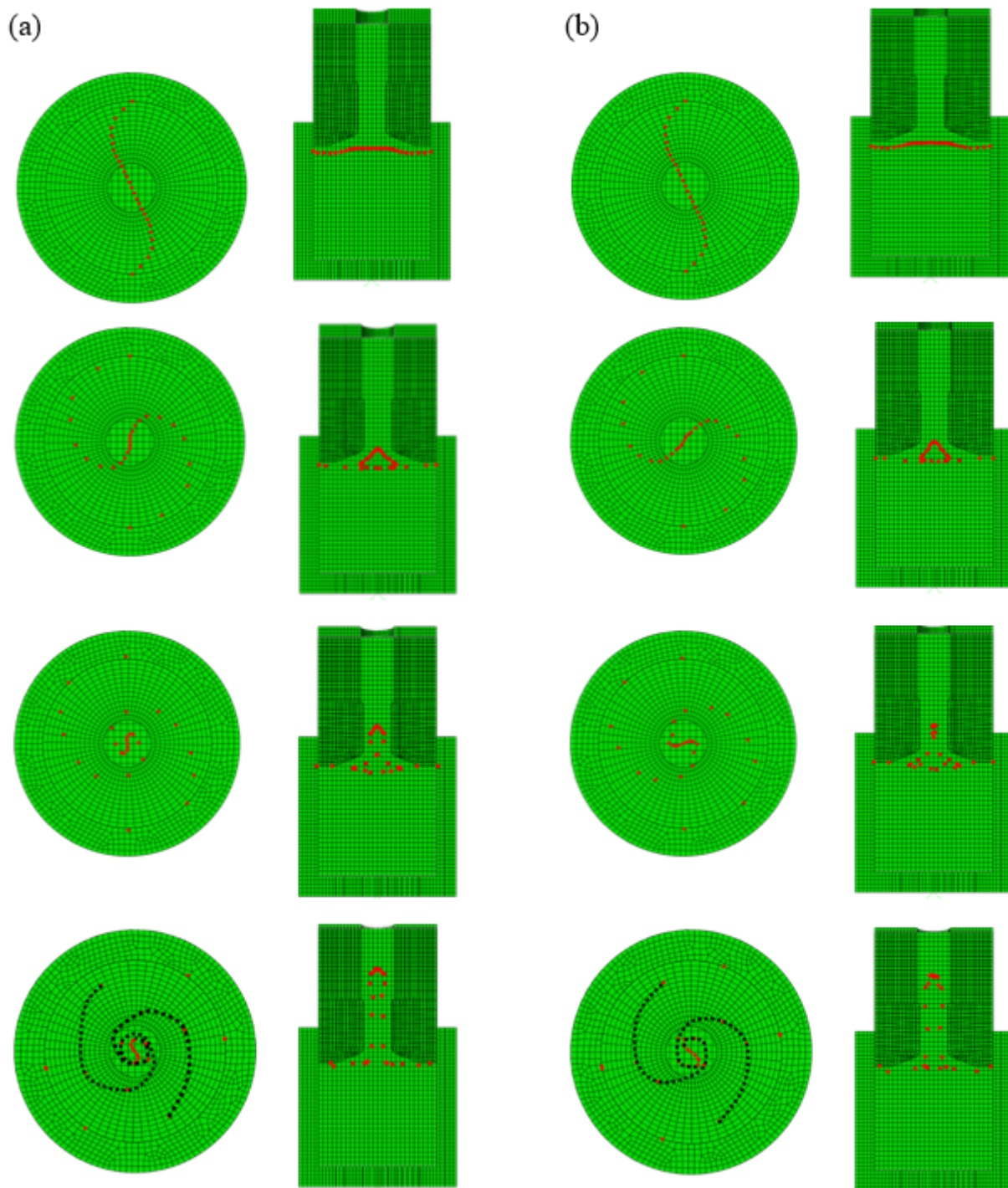
Figure 14

The material flow pattern from top and front views at different time intervals. (a) 800 rpm and 40 mm/min, and (b) 500 rpm and 40 mm/min.